Characterisation of the filter inlet system on the BAE-146 research aircraft and its use for size resolved aerosol composition measurements

Alberto Sanchez-Marroquin[1], Duncan H. P. Hedges[1], Matthew Hiscock[2], Simon T. Parker[3], Philip D. Rosenberg[1], Jamie Trembath[4], Richard Walshaw[1], Ian T. Burke[1], James B. McQuaid[1], Benjamin J. Murray[1]

[1]School of Earth and Environment, University of Leeds, Woodhouse Lane, Leeds, LS2 9JT, UK

[2] Oxford Instruments NanoAnalysis, High Wycombe, HP12 3SE

[3]Defence Science and Technology Laboratory, Salisbury, SP4 0JQ, UK

[4]Facility for Airborne Atmospheric Measurements, Building 146, Cranfield University, College Road, Cranfield, Bedford MK43 0AL

Abstract

Atmospheric aerosol particles are important for our planet's climate because they interact with radiation and clouds. Hence, having characterised methods to collect aerosol from aircraft for detailed offline analysis are valuable. However, collecting aerosol, particularly coarse mode aerosol, onto substrates from a fast moving aircraft is challenging and can result in both losses and enhancement in particles. Here we present the characterisation of an inlet system designed for collection of aerosol onto filters on board the Facility for Airborne Atmospheric Measurements (FAAM) BAe-146 research aircraft. We also present an offline Scanning Electron Microscopy (SEM) technique for quantifying both the size distribution and size resolved composition of the collected aerosol. We use this SEM technique in parallel with online underwing optical probes in order to experimentally characterise the efficiency of the inlet system. We find that the coarse mode aerosol is sub-isokinetically enhanced, with a peak enhancement at around 10 µm up to a factor of three under typical operating conditions. Calculations show that the efficiency of collection then decreases rapidly at larger sizes. In order to minimise the isokinetic enhancement of coarse mode aerosol we recommend sampling with total flow rates above 50 L min^{-1}; operating the inlet with the bypass fully open helps achieve this by increasing the flow rate through the inlet nozzle. With the inlet characterised, we also present single particle chemical information obtained from X-ray spectroscopy analysis which allows us to group the particles into composition categories.

1 Introduction

Atmospheric aerosol particles are known to have an important effect on climate through directly scattering or absorbing solar and terrestrial radiation as well as through indirect effects such as acting as Cloud Condensation Nuclei (CCN) or Ice-Nucleating Particles (INPs) (Albrecht, 1989; DeMott et al., 2010; Haywood and Boucher, 2000; Hoose and Mohler, 2012; Lohmann and Diehl, 2006; Lohmann and Gasparini, 2017). Aerosol particles across the fine (diameter < 2 µm) and coarse (> 2 µm) modes are important for these atmospheric processes. For example, aerosol in the accumulation mode are important CCN (Seinfeld and Pandis, 2006), whereas supermicron particles are thought to contribute substantially to the INP population (Creamean et al., 2018; Mason et al., 2016; Pruppacher and Klett, 1997). Hence, being able to sample across the fine and coarse modes is required to understand the role aerosol play in our atmosphere. However, sampling aerosol particles without biases can be challenging, this being especially so on a fast moving aircraft (Baumgardner et al., 2011; Baumgardner and Huebert, 1993; McMurry, 2000; Wendisch and Brenguier, 2013).

It is necessary to sample aerosol from aircraft because in many cases aircraft offers the only opportunity to study aerosol and aerosol-cloud interactions at cloud relevant altitudes (Wendisch and

44   Brenguier, 2013). However, the relatively high speeds involved present a set of unique challenges for
45   sampling aerosol particles. This is especially so for coarse mode aerosol which are prone to both losses
46   as well as enhancements because their high inertia inhibits their ability to follow the air stream lines
47   when they are distorted by the aircraft fuselage and the inlet (Brockmann, 2011; McMurry, 2000; von
48   der Weiden et al., 2009). Therefore, inlet design and characterisation becomes extremely important
49   when sampling aerosol particles.

50   In this study we characterise the inlet system used for collecting filter samples (known as the Filters
51   system) on board the UK's BAe-146-301 Atmospheric Research Aircraft, Facility for Airborne
52   Atmospheric Measurements (FAAM). This system has been used for many years, but its
53   characterisation has been limited (Chou et al., 2008; Price et al., 2018; Ryder et al., 2018; Young et al.,
54   2016). Our goal in this characterisation work was to define recommendations for the use of the inlet
55   system to minimise sampling biases and define the size limitation and the biases that exist. While the
56   filter samples could be used for a variety of offline analyses, we have done this characterisation with
57   two specific goals in mind: firstly, we want to use this inlet system for quantification of INP (the
58   technique for this analysis has been described previously (Price et al., 2018) and will not be further
59   discussed here); secondly, we have adapted and developed a technique for quantification of and the
60   size resolved composition of the samples using Scanning Electron Microscopy (SEM). We use this
61   technique in order to test the inlet efficiency. These experiments are underpinned by calculations
62   which elucidate how the biases are impacted by variables such as flow speed, angle of attack and use
63   of the bypass system. Finally we present an example of the use of the inlet for determining the size
64   resolved composition of an aerosol sample collected from the FAAM aircraft.

65   **2. Description and theoretical sampling characteristics of the filter inlet system on the Facility for**
66   **Airborne Atmospheric Measurements (FAAM) aircraft**

67   Ideally, aerosol particles would be sampled through inlets without enhancement or losses. However,
68   this is typically not the case when sampling from aircraft, hence it is important to know how the size
69   distribution of the aerosol particles is affected by the sampling. Generally, an aircraft moves at high
70   velocities with respect to the air mass that it is being sampled. During sampling on the FAAM aircraft
71   the indicated airspeed is 100 m s^{-1}, which yields to a true airspeed that fluctuates between 100 and
72   120 m s^{-1}. The air mass has to decelerate when passing through the inlet (Baumgardner and Huebert,
73   1993) and this tends to result in inertial enhancement of coarse mode aerosol. There are also losses
74   through the inlet system, for example, through inertial impaction at bends or gravitational settling in
75   horizontal sections of pipework. These inlet characteristics need to be considered if the subsequent
76   analysis of the aerosol samples is to be quantitative. In this section we first describe the existing inlet
77   system and then present theoretical calculations for the size dependent losses and enhancements.

78   **2.1 Description of the Filters system**

79   The FAAM BAe-146 aircraft has two identical inlets for sampling aerosol onto filters for offline analysis.
80   This inlet system was used to sample aerosol particles on board of the C-130 aircraft before being
81   installed on the FAAM BAe-146 (Andreae et al., 1988; Andreae et al., 2000; Talbot et al., 1990), and it
82   has been used to sample aerosol particles on the FAAM Bae-146 e.g. (Chou et al., 2008; Hand et al.,
83   2010; Price et al., 2018; Young et al., 2016). A diagram of the inlet system can be seen in Fig. 1. The
84   two parallel inlet and filter holder systems, which each have a nozzle whose curved leading edge
85   profile follows the criteria for aircraft engine intakes at low Mach numbers (low speeds when
86   compared with the speed of sound; for FAAM during sampling this is ~0.3), and it is designed to avoid
87   the distortion of the pressure field at the end of the nozzle, flow separation and turbulence (Andreae
88   et al., 1988; Talbot et al., 1990). The inlet has a bypass to remove water droplets or ice crystals through

89   inertial separation and also enhance the flow rate at the inlet nozzle (Talbot et al., 1990). The flow
90   through the bypass (bypass flow) can be regulated using a valve and it is driven passively by the
91   pressure differential between the ram pressure inlet and the Venturi effect on the exhaust. After
92   turning inside the aircraft, the airstream containing the aerosol particles continue through the filter
93   stack after passing a valve. The air flow through the filter (filter flow) is measured by a mass flow
94   meter, which measures the sampled air mass and reports it in equivalent litres at standard conditions
95   (273.15 k, 1013.529 hPa). The uncertainty for this flow meter is 1% of the full scale (400 L min^{-1}). The
96   effect of water vapour on the mass flow has not been corrected since its effect is negligible. The signal
97   is integrated by an electronics unit to give the total volume of air sampled for any given time period.
98   There is also a valve between the pump and the flow meter. The valve allows the inlet and pump to
99   be isolated from the filter holder when changing the filter. The system uses a double-flow side channel
100   vacuum pump model SAH55 made by Elmo Rietschle (Gardner Denver Inc.), aided by the ram effect
101   of the aircraft. The flow rate at the inlet nozzle (total flow) is the sum of the bypass flow and the filter
102   flow. The inlet nozzle is located at 19.5 cm of the aircraft fuselage, so the sampling is carried out in
103   the free stream, outside the boundary layer.

104

105   **2.2 Sampling efficiency**

106   We present theoretical estimates of the losses and enhancements due to aspiration, inlet inertial
107   deposition, turbulent inertial deposition, inertial deposition in bends and gravitational effects in Fig
108   2a. We used the term 'efficiency' to define the ratio between the number concentrations of particles
109   after they were perturbed relative to the unperturbed value. If the efficiency is above one, the number
110   of particles is enhanced whereas if it is below 1, particles are lost before they reach the filter.

111   The sampling efficiency of any inlet depends on the flow rates and the flow regime (laminar vs
112   turbulent), the pressure and the temperature. Filter flow rates for 0.4 μm polycarbonate filters
113   normally vary between 10 and 50 L min^{-1} depending on altitude (see section 2.3 for a discussion of
114   flow rates). The bypass flow rate (when it is fully open) can go up to 35 L min^{-1} at 30 m and 22 L min^{-1}
115   at 6 km (volumetric L at standard conditions: 273.15 k, 1013.529 hPa), but it is not measured routinely.
116   In the 2.5 cm diameter section of the inlet, just after the inlet nozzle, the Reynolds number (Re) is
117   below the turbulent regime threshold (Re > 4000) for flow rates below 65 L min^{-1}. For larger values of
118   Re, the flow starts becoming turbulent. At the inlet nozzle, where the diameter 0.7 cm, Re is above
119   4000 for flow rates above 20 L min^{-1}, so the flow is briefly in the turbulent regime at the inlet for most
120   sampling conditions. Fully characterising the losses and enhancements of aerosol particles passing
121   through the inlet is very challenging since there are several aerosol size dependent mechanisms that
122   can enhance or diminish the amount of aerosol particles that arrive at the filter.

123   Here we have considered the most important of these mechanisms (von der Weiden et al., 2009) in
124   order to estimate the inlet efficiency (see Fig. 2a) for a total flow rate of 50 L min^{-1} (all the flow rates
125   of our calculations are given in L min^{-1} at standard conditions: 273.15 k, 1013.529 hPa). These loss
126   mechanisms and their importance in this inlet system are defined as follows (a discussion on the
127   choice of equations, how they have been applied and the excluded mechanisms can be found in
128   Appendix A):

129   *Aspiration efficiency* has been calculated using the empirical equation as develop in Belyaev and Levin
130   (1972) and Belyaev and Levin (1974). As one can see in Fig. 2a this mechanism enhances aerosol
131   particles, tending to 1 for small diameters and to the ratio in between the air speed inside the nozzle
132   and outside the aircraft for large ones.

133   *Inlet inertial deposition* has been characterised using the equation given in Liu et al. (1989) which
134   quantifies this effect. In Fig. 2a one can see that it produces some losses, with a minimum efficiency
135   of down to 50% for sizes about 6 µm, without affecting the lower and upper limit of the aerosol size.

136   *Turbulent inertial deposition* occurs throughout the whole inlet system for flow rates above 65 L min^{-1}
137   and only occurs in the inlet nozzle for flow rates below this threshold. We have used the equation
138   given by Brockmann (2011) in order to account for this mechanism. In Fig. 2a one can see an example
139   of the turbulent inertial losses at the nozzle. This mechanism gradually decreases the efficiency for
140   aerosol particles above 5 µm.

141   *Bending inertial deposition* has been characterised using the equation given in (Brockmann, 2011).
142   This efficiency mechanism, which can be seen in Fig. 2a, adds a size cut off with a D50 value at ~25
143   µm.

144   *Gravitational settling* of aerosol particles was considered using the equations developed in Heyder
145   and Gebhart (1977) and Thomas (1958), as stated in Brockmann (2011). This efficiency mechanism
146   adds another size cut off with a D50 value of 35 µm, as one can see in Fig. 2a*.

147   *Diffusional efficiency and filter collection efficiency* have not been included in Fig. 2. The first
148   mechanism has been calculated using the analytical equation given by Gormley and Kennedy (1948),
149   but it is not shown since it is very close to 1 for all the considered size range. For the filter types and
150   pore sizes we used, filter collection efficiency is also close to a 100% across the relevant size range
151   (Lindsley, 2016; Soo et al., 2016).

152   *Anisoaxial losses* are losses produced by the fact that the inlet is not aligned with the velocity of the
153   air mass, being offset by an angle, θ (related to the angle of attack). The anisoaxial sampling can affect
154   the sub-isokinetic efficiency, but using the equations given by Hangal and Willeke (1990a), we
155   calculated that this effect is minimal for our conditions. In addition, anisoaxial sampling can lead to
156   inertial losses when particles impact the inner walls of the inlet. This phenomena has been quantified
157   using the equations in Hangal and Willeke (1990b) and the results can be seen in Fig. 3. As one can
158   see, this efficiency mechanism adds an additional cut off for large aerosol particles (with values of D50
159   down to ~20 µm), depending on the value of the sampling angle.

160   One can see all the efficiency mechanisms combined for four different flow rates in Fig. 2b. These have
161   been derived by multiplying all the efficiencies for the individual mechanisms. This overall efficiency
162   is the ratio between the particles that reach the filter and the particles in the ambient air. The
163   sampling efficiency for the submicron aerosol is close to 1. At sizes above 1 µm, the different loss
164   mechanisms become increasingly significant. For the range of flow rates considered, the efficiency
165   approaches zero between 20 and 50 µm, with D50 values in between ~10 and ~33 µm (although these
166   values could be lower under certain values of angles of attack if considering the anisoaxial losses of
167   from Fig. 3, which haven't been included). For the 80 L min^{-1} case, the flow is turbulent through all the
168   pipe, leading to enhanced losses of coarse aerosol particles which partially compensate the sub-
169   isokinetic enhancement of the system.

170   One can also see that the sub-isokinetic enhancement of large aerosol particles increases when
171   decreasing the flow rate of the system. This effect is about a factor 3.5 for 10 µm particles when
172   sampling at 15 L min^{-1}, but only a factor of two at 50 L min^{-1}. The sub-isokinetic enhancement can be
173   mitigated using the bypass, which enhances the flow through the nozzle. This can be seen in Fig. 2c
174   where one can see a comparison between the total efficiency of a 20 L min^{-1} flow rate through the
175   filters with no bypass flow and the same case when the bypass is open. Since the considered bypass
176   flow is comparable to the flow rate through the filters, the difference between the total flows for the

177 two cases is approximately a factor 2. As a consequence, the maximum sub-isokinetic enhancement
178 of large aerosol particles is almost a factor 2 larger when sampling with the bypass closed. Hence, the
179 sub-isokinetic enhancement can be reduced by keeping the bypass fully open.

180

181 **2.3 Sampling flow rate**

182 Here we show flow rate data from four field campaigns in order to examine how the flow rate of the
183 filter inlet system varied based on different factors. We have used the data collected during the ICE-D
184 campaign, in Cape Verde during August 2015 (Price et al., 2018). The rest of the data is from some
185 flight test carried out during 2017 and 2018, and three field campaigns. The first one was EMERGE,
186 based in south east England, in July 2017. The second one was VANAHAEIM, based in Iceland in
187 October 2017. The last campaign was MACSSIMIZE, based in Alaska in 2018. The flow rate of the inlet
188 system is known to vary with altitude, with a lower flow rate at high altitudes because of the reduced
189 pressure differential across the filter and the fact that the pump efficiency decreases at low pressure.
190 In addition, it changes depending on the filter type and the pore size.

191 In Fig. 4, where all the flow rate data has been presented, one can see that the flow rate tends to
192 decrease with altitude and change with filter type as expected, but the flow rates are not always
193 consistent for each altitude and filter type, varying up to a factor two for each filter
194 type/line/altitude/campaign. The filter type effect on flow rate can be seen in Fig. 4, where the
195 average flow rate for 0.4 µm polycarbonate filters is about twice the flow rate of the 0.45 µm PTFE
196 filters. In order to investigate the inconsistency in the flow rate at each altitude, we analysed the flow
197 rate data by comparing it with different parameters (ambient air and cabin temperature, ambient air
198 and cabin pressure, wind direction and speed with respect to the aircraft movement), but there was
199 no correlation with any of these variables. Different mesh supports were used, but this does not affect
200 the flow rate significantly according to some ground based tests. We checked the flow rate through
201 each sampling period and found it did not change over time on a particular filter set (even after
202 stopping the sampling and starting it again). In addition, we performed some tests on the ground and
203 during flights to study the effect of potential leaks by inserting paper disks of the same dimension as
204 the filters in the filter holders and found no evidence of leaks in the system.

205 We conclude that this variability in the flow rate comes from variability in the pump performance in
206 combination with subtle differences in individual filter pairs. The side displacement pump is not the
207 ideal pump for this system and operates at its maximum capacity. Hence, we suggest that to improve
208 the performance of the system that flow rates are actively controlled and also the side displacement
209 pump is replaced with a more appropriate design. This would also have the advantage that flow rates
210 would be maintained at smaller pressure drops and allow sampling at higher altitudes.

211

212 **3. FAAM underwing optical particle counters**

213 Later in the paper we compare results from the underwing optical particle counters with our electron
214 microscope derived size distributions, hence we describe the optical instruments here. The FAAM BAe-
215 146 aircraft operates underwing optical particle counters to measure aerosol size distributions. These
216 include the Passive Cavity Aerosol Spectrometer Probe 100-X (PCASP) and the Cloud Droplet Probe
217 (CDP). The PCASP measures particles with diameters in the approximate range 0.1-3 µm and the CDP
218 measures the particles with diameters in the range of 2-50 µm. These instruments are placed outside
219 the aircraft fuselage, below the wings. These instruments and the methods for calibration are
220 described in (Rosenberg et al., 2012). All the PCASP-CDP data shown here has been extracted from

the FAAM cloud datasets corresponding to each specific flight via the Centre for Environmental Data Analysis.

The instruments were calibrated and had optical property corrections applied as per Rosenberg et al. (2012). We used a refractive index of 1.56 + 0i and a spherical approximation (Mie theory) in the optical property corrections. In Fig. 5, one can see a sensitivity test on the refractive index value we used in order to examine how variability in refractive index affect the bin centres position, their width, and therefore the size distribution obtained from the PCASP and CDP. As one can see in Fig. 5a, modification of the real part of the refractive index from 1.5 to 1.7 can change the position of the PCASP bin centres up to a factor 1.5, but its effect on the CDP is not significant. When varying the imaginary part of the refractive index from 0 to 0.01, the bin centre positions of the first half of the range of the PCASP and CDP do not change but it can change the position of the bins of the end of the range of both instruments (less than a factor 1.5). However, for the purposes of this work, the differences produced by the variation in the refractive index are not large enough to modify the conclusions of the analysis, therefore we use a value of 1.56 + 0i.

The chosen refractive index range for this sensitivity analysis can be justified on the basis that the SEM compositional analysis showed that the composition of the aerosol samples used in this study was very heterogeneous, dominated by carbonaceous particles (biogenic, organic and black carbon) and with some contributions of mineral dust and other particle types. Values of the real part of the refractive index in the 1.5 to 1.6 range are compatible with sodium chloride and ammonium sulphate (Seinfeld and Pandis, 2006), as well as most mineral dusts (McConnell et al., 2010). The range is very close to values for the real part of the refractive index of organic carbon but below the values for black carbon (Kim et al., 2015). As a consequence, the refractive index choice might not be accurate for a black carbon dominated sample. However, black carbon is highly unlikely to dominate in the size range where a value of the real part of the refractive index of 1.7 dramatically changes the size distribution (diameters above 0.5 µm) (Seinfeld and Pandis, 2006), so our refractive index choice is valid. In Fig. 5b one can see that changing the imaginary part of the refractive index from 0 to 0.01 only produces small changes in the distribution. The imaginary part of the refractive index of many aerosol types as sodium chloride, sulphates and mineral dust falls within the shown range (Seinfeld and Pandis, 2006), (McConnell et al., 2010). For values of the imaginary part of the refractive index above 0.01 (not shown in the image), the size distribution dramatically changes for sizes above 1 µm (but not for smaller values of it), overlapping and disagreeing with the CDP. However, values above 0.01 in the imaginary part of the refractive index are only associated with strongly absorbing aerosol like black carbon, which will dominate only in the submicron sizes (Seinfeld and Pandis, 2006). The submicron part of the size distribution doesn't change for values of the imaginary part of the refractive index above 0.01, so our refractive index choice is still acceptable even for samples with significant contributions from black carbon in submicron sizes.

For the PCASP-CDP, we have considered two uncertainty sources. The first one is the Poisson counting uncertainty in the number of particles in each bin and the second one is the uncertainty in the bin width that is given by the applied optical property corrections. Both sources have been propagated in order to obtain the errors of dN/dlog$D$p and dA/dlog$D$p. The errors in the bin centre position were given by the calibration. In order to avoid the problems with the transition in between different gain stages in the PCASP, some bins were merged or eliminated (5 and 6 as well as 15 and 16 were merged, while the bin 30 was eliminated), as indicated by Rosenberg et al. (2012). Other uncertainties such as the refractive index assumption or particle shape effect, as well as the uncertainty in the bin position haven't been regarded in this study. Sampling biases haven't been quantified or corrected yet so they

266 haven't been included. The size distributions produced by the PCASP-CDP have been taken as a
267 reference value for the purposes of this study.

268

269 **4. Scanning Electron Microscopy technique for aerosol characterization**

270 Scanning Electron Microscopy is used in order to study composition and morphology of aerosol
271 particles, in a similar way to previous works such as Krejci et al. (2005), Kandler et al. (2007), Chou et
272 al. (2008), Kandler et al. (2011), Young et al. (2016), Price et al. (2018) and Ryder et al. (2018). We use
273 a Tescan VEGA3 XM scanning electron microscope (SEM) fitted with an X-max 150 SDD Energy-
274 Dispersive X-ray Spectroscopy (EDS) system controlled by an Aztec 3.3 software by Oxford
275 Instruments, at the Leeds Electron Microscopy and Spectroscopy Centre (LEMAS) at the University of
276 Leeds. In order to get data from thousands of particles in an efficient way, data collection was
277 controlled by the AztecFeature software expansion.

278 Aerosol particles were collected with the filter inlet of the FAAM aircraft on polycarbonate track
279 etched filters with 0.4 μm pores (Whatman, Nucleopore). Samples for SEM are usually coated with
280 conductive materials in order to prevent the accumulation of charging on the sample surface (Egerton,
281 2005). For aerosol studies, materials like gold (Hand et al., 2010), platinum (Chou et al., 2008), or
282 evaporated carbon (Krejci et al., 2005; Reid et al., 2003; Young et al., 2016) have been used. When it
283 comes to choosing which signal to detect, some previous studies used mainly backscattered electrons
284 (Gao et al., 2007; Kandler et al., 2007; Kandler et al., 2011; Kandler et al., 2018; Price et al., 2018; Reid
285 et al., 2003; Young et al., 2016) and some others choose secondary electrons (Hamacher-Barth et al.,
286 2013; Krejci et al., 2005). We started the development of this analysis using a carbon coating and the
287 backscattered electron detector. This technique produced reproducible images and almost no
288 artefacts from the pore edges, consistent with Gao et al. (2007). However, we noticed that we
289 sometimes undercounted a significant fraction of the small carbon based particles (this strongly
290 depended on the sample), which looked transparent under the backscattered electron imaging but
291 not under the secondary electron detector, as seen in Fig. 6. This likely happened because the contrast
292 in the secondary electron images mainly depends on the topography of the sample whereas the
293 contrast in the backscattered electron images depends on the mean atomic number of each sample
294 phase (Egerton, 2005). Since the polycarbonate filters are made of C and O, particles containing only
295 these elements in a similar proportion to the background did not exhibit a high contrast under the
296 backscattered electron detector (Laskin and Cowin, 2001). However, when using secondary electron
297 imaging with carbon coatings, images were less reproducible and contained artefacts from the pore
298 edges, probably resulting from charging or topographical effects. We found that coating the samples
299 with 30 nm of iridium helps to improve the secondary electron image reproducibility and reduced the
300 pore edge artefacts as well as allowing us to locate small organic particles. An increase in the size of
301 the particle as a consequence of the coating may introduce an uncertainty in the size of the smallest
302 particles. An additional advantage of using Ir is that the energy dispersive X-ray spectrum of Ir does
303 not overlap greatly with the elements of interest.

304 In the SEM the sample was positioned at a working distance of 15 mm. The SEM's electron beam had
305 an accelerating voltage of 20 KeV and a spot size chosen to produce the optimum number of input
306 counts in the EDS detector. Images are taken at two different magnifications with a pixel dwell time
307 of 10 μs and a resolution of 1024 x 960 pixels per image. High magnification images (40 nm per pixel
308 or smaller) were used to identify particles down to 0.3 or 0.2 μm depending on the sample, and
309 medium magnification images (about 140 nm per pixel) are used to identify particles down to 1 μm. A
310 brightness threshold with upper and lower limits that correspond to pixels of certain shades of grey

311 was manually adjusted for each image by the operator to discriminate particles from the background.
312 Based on the manually set brightness threshold, AztecFeature identified the pixels that fall within the
313 limits as aerosol particles and calculated several morphological properties of the particle as cross
314 sectional area, length, perimeter, aspect ratio, shape factor or equivalent circular diameter. The
315 equivalent circular diameter is defined as $\sqrt{(4\,A\,\pi^{-1})}$, where A the cross sectional area of the aerosol
316 particle. This equivalent circular diameter has not been corrected or transformed into an optical or
317 other equivalent diameter.

318 For this analysis we placed a section of the 47 mm filter on a 25 mm stub. In order to collect
319 morphological and chemical information from a few thousand particles, we only scanned a fraction of
320 the filter (typically up to 1% of the filter at low magnification and up to 0.01% for high magnification).
321 We collected information from 5 to 20 different areas, and each area consisted of a montage of several
322 SEM images. In Fig. 7 one can see the radial distribution of aerosol particles on top of a filter collected
323 using the inlet system. In spite of some fluctuations (which are up to a factor 3 and appear to be
324 random), one can see that the particles are homogenously distributed all over the central ~30 mm of
325 the filter. As a consequence, the areas were chosen by the user from all over the surface of the
326 selected fraction of the filter. Each area was selected in the software, manually adjusting the particle
327 detection threshold. The Z position of the stage was also adjusted manually for each image in order
328 to produce properly focused images. After doing this, the image scanning and EDS acquisition was
329 performed in an automated way. Morphological information was recorded for all particles with an
330 equivalent circular diameter greater than the specified size threshold (typically 0.2 or 0.3 µm).

331 EDS analysis was restricted to the first 12 or 15 particles detected in each image. This reduces the
332 likelihood of image defocusing over the SEM automated run. The software performed EDS in the
333 centre of the particles, obtaining around 50,000 counts per particle. The raw data for any given particle
334 were matrix corrected and normalised by the AZtec software to produce element weight percent
335 values with a sum total of 100%, using a value of the confidence interval of 2 (a further discussion on
336 the confidence interval can be seen in the Appendix C). Then particles were categorised based on their
337 chemical composition using a classification scheme which can be created and modified within the
338 AztecFeature software. The characteristic X-rays taken at one point are emitted by a certain
339 interaction volume which is bigger than some of the analysed particles (typically < 2 µm^3, decreasing
340 with atomic number and increasing with incident electron energy). As a consequence, a part of the X-
341 ray counts attributed to each particle come from the background (C and O from the polycarbonate
342 filter and Ir from the coating) and the weight percentages obtained from the X-ray spectra do not
343 match the actual weight percentages of the particle itself. As a consequence, when categorising the
344 particles based on their composition, we only use the presence or absence of certain elements, and
345 the ratio between the weight percentages of non-background elements. The classification scheme
346 works by checking if the composition of each particle falls within a range of values which are manually
347 defined by the user. Particles not matching the first set of rules are tested again for a second set of
348 rules, and so on, until reaching the last set of rules. A few sets of rules can be merged into a category.
349 In the supplementary information (Fig. S3), we give the details of the 32 sets of rules used, which are
350 then summarised into 10 composition categories. A description of the most abundant elements in
351 each category and an interpretation of these categories is included in Appendix B.

352 The detection of particles has certain limitations. The edges of the pores can look brighter than the
353 rest of the filter in the SE images (probably because they consist of a larger surface area from which
354 secondary electrons can be generated, hence a larger signal). As a consequence, they can look like
355 ~0.2 µm particles, which is the main reason why particles below 0.3-0.2 µm (depending on the sample)
356 are not included in this analysis. These artefacts had a chemical composition similar to the filter, so

they were labelled as "Carbonaceous" by the classification scheme, falling at the same category as most biogenic and black carbon particles. However, these artefacts were only around 1 to 10 percent depending on the sample. If they appear in larger quantities, they can be removed manually after or during the analysis. Another limitation arises from the fact that some aerosol particles did not have sufficient brightness in the SE image and were not detected as a particle. This happens more frequently for submicron particles (especially the ones closer to the limit of detection), but it can also happen with some coarse mode aerosol particles, particularly if they are only composed of Na and Cl or S. This issue can be addressed if necessary by setting a very low limit of detection, which adds lots of artefacts as well as the low brightness particles, and then removing the artefacts manually (the artefacts can be easily identified by the user). In other infrequent instances, only a fraction of the particle had a brightness above the threshold, so they were detected as a smaller particle or multiple smaller particles, or if two particles are close enough, they can be detected as a single larger particle. However, we feel that in the vast majority of the cases a representative cross sectional area of the particle was picked by the software.

Blank polycarbonate filters can contain some particles on them from manufacturing or transport before being exposed to the air. In addition, handling and preparing the filters can introduce additional particles to it. In order to assess these artefacts, we scanned a few clean blank filters. We also examined a filter that had been brought to the flight, loaded in the inlet system (but not exposed to a flow of air), and then stored at -18 $^{\circ}$C for a few months (like most of the aerosol samples on filters). The results of both the handling blank and the blank can be seen in Fig. S2. The number of particles is typically about the order of magnitude of one particle per 100 by 100 µm square, which is more than an order of magnitude below all the samples in this study (apart from the sample shown in Fig 9c which was taken in a very low aerosol environment, where it is only about a factor 2). In Fig. S2 one can see that about half of particles found in both blank filters and the handling blank belong to the metal rich category. However, further examination of the composition of these metal rich particles revealed that almost all of them were Cr rich particles (about 97 % in the case of the blank filters and about 96% in the case of the handling blank). As a consequence, we excluded all the Cr rich particles from the analysis of atmospheric aerosol. By doing this, we make sure that we exclude about half of the artefacts of the analysis. There was a contribution of mineral dust origin particles (Al-Si rich, SI rich and Si only) for sizes in between 0.7 and 5 µm in the handling blank (less than 10% of the number in the handling blanks). Generally, the composition of the particles present in the blank filters and in the handling blank was very similar, suggesting that most of these artefacts are not produced by the loading, manipulation and storage of the filter.

5. Inlet characterisation and sampling efficiency using Scanning Electron Microscopy

In order to experimentally test the inlet efficiency, to complement the efficiency calculations presented in Section 2.2, we have used SEM to quantify the size distribution of particles collected on filters (Sect. 4) and compare this with the measurements from the under-wing optical probes (Sect. 3). The calculations in Sect. 2.2 suggest that there is an enhancement of the coarse mode aerosol particles, which is larger when sampling with the bypass closed. To test this we have collected aerosol onto 0.4 µm pore size polycarbonate filter in both lines in parallel and show these results in Fig. 8. In one of the lines, the bypass was kept open, and in other line the bypass was kept closed. Using our SEM approach described in the Sect. 4, we calculated the size distribution of the aerosol particles on top of each filter. We compared these size distributions with the ones measured by the underwing optical probes (PCASP-CDP), as described in Sect. 3. We performed the comparison twice in two different test flights based in the UK.

403 One can see that the concentration of aerosol particles measured by the SEM on the filters was higher
404 than the particles detected by the optical probes for sizes above ~8 µm in Fig. 8 (reaching about an
405 order of magnitude in number around 10 µm in both cases). These results are consistent with Price
406 et al. (2018) and Ryder et al. (2018), where they observed an enhancement of coarse aerosol particles
407 in mineral dust dominated samples collected close to Cape Verde. In addition, the enhancement was
408 larger when sampling with the bypass closed (about a factor 2-3). The results of these comparisons
409 are in qualitative agreement with the theoretical calculations in Sect. 2.2, i.e. that the sub-isokinetic
410 enhancement is reduced with the bypass open.

411 After establishing that having the bypass open produces a more representative sampling of coarse
412 mode aerosol we then had the bypass open for the subsequent sampling. In Fig. 9 we have presented
413 some other bypass open SEM size distributions compared with the PCASP-CDP data from three
414 different aerosol samples in contrasting locations. Since these data were taken during the scientific
415 field campaigns and not test flights, we only collected one polycarbonate filter for SEM since the other
416 line was used for INPs analysis on Teflon filters (not shown here). In Fig 9a, one can see a sample
417 collected in the UK where there is an enhancement of the coarse mode which reaches almost an order
418 of magnitude at 10 µm. The sample shown in Fig 9b was collected in Iceland, and the enhancement of
419 coarse aerosols can be seen through most of its range, reaching even the first two bins of the
420 submicron aerosol range. In Fig 9c one can see a sample collected in North Alaska where the coarse
421 mode aerosol concentration was one to two orders lower than the examples from the UK and Iceland.
422 In this case the SEM size distribution is only about a factor 2 above the size distribution of the handling
423 blank, nevertheless the SEM and optical probes both produce similarly low numbers of coarse mode
424 aerosol. The low number concentration results in the lack of data in the SEM above 7 µm and the large
425 uncertainties in the PCASP-CDP above 1.5 µm. We do not observe a coarse mode enhancement in this
426 sample, probably because of the low aerosol concentration in the size range where we expect the
427 largest biases and large uncertainties.

428 In the submicron range, one can see that in all the comparisons shown in Fig. 8 and Fig. 9 there is
429 sometimes an undercounting in the SEM size distribution when compared with the optical probes.
430 Generally, the undercounting increases with decreasing size and reaches an order of magnitude or
431 more, as one can see in Fig. 8, Fig. 9a and Fig. 9c; this is qualitatively similar to Young et al. (2016).
432 There are several potential reasons for this. We can rule out particles simply being lost by passing
433 through the 0.4 µm polycarbonate filters, since they are known have a high collection efficiency
434 (Lindsley, 2016; Soo et al., 2016), although some of them might deposit inside the pores and therefore
435 not be detected. In addition, it is likely that some small particles are not sufficiently bright to be
436 detected, despite the fact we made efforts to mitigate this problem with the use of secondary
437 electrons and the Ir coating (see figure 6). Also, volatilization of certain types of aerosol particles
438 (which are more abundant in the submicron fraction (Seinfeld and Pandis, 2006)) can occur during
439 heating (in this case produced by deceleration of the flow in the inlet) or sampling (Bergin et al., 1997;
440 Hyuk Kim, 2015; Nessler et al., 2003) and this effect could be enhanced by the fact that samples are
441 exposed to high vacuum during the SEM analysis. In addition, the SEM techniques measure the dry
442 diameter and the optical probes measure the aerosol diameter at ambient humidity. This hygroscopic
443 effect shifts the dry size distributions to smaller sizes, which might also explain part of the
444 disagreement (Nessler et al., 2003; Young et al., 2016). Disagreement in the measurements can also
445 be produced by the fact that the techniques are measuring different diameters (optical and
446 geometric).

447 Some of the PCASP size distributions contain some 'bumps' (particularly above 2 µm), but it is not
448 possible to address if they are physical or just an artefact produced by the refractive index correction

449 (Rosenberg et al., 2012). Given the uncertainties on both techniques and the fact that they measure
450 different diameters (optical diameter in the case of the PCASP-CDP and geometric equivalent circular
451 diameter in the case of the SEM), this comparisons cannot be used to quantify the biases in the system,
452 but can be used to make a qualitative comparison. For similar reasons, the SEM data has not been
453 corrected using the theoretical efficiency.

6. Application to samples collected from the atmosphere above S.E. England and North Alaska

455 The SEM technique to produce size resolved composition of aerosol samples described in Sect. 4 has
456 been applied to samples collected from the FAAM aircraft in various locations. In Fig. 10 we show an
457 example of some of the capabilities of this technique applied to a sample collected in S. E. England.
458 The purpose of this section is purely to give examples of the capabilities of the technique, further
459 analysis is planned for subsequent papers. The fraction of particles corresponding to each
460 compositional category described in Appendix B for each size can be seen in Fig. 10a and the
461 corresponding number size distribution of each composition category can be seen in Fig. 10b. By
462 looking at this analysis, one can see that the sample carbonaceous aerosol particles made a substantial
463 contribution to the number across the full distribution and there was a clear mineral dust mode (Si
464 only, Si rich Al-Si rich and Ca rich) for particles larger than about 1 μm. There was also a smaller
465 contributions of metal rich and S rich aerosol particles, particularly in the fine mode. A potentially
466 useful application of the size resolved composition is calculating the surface area or mass of an
467 individual component of a heterogeneous aerosol. As an example, we have grouped the mineral dust
468 categories Si only, Si rich Al-Si rich and Ca rich to produce the surface area size distribution of mineral
469 dust (and potentially ash) in Fig. 10c.

470 In Fig. 11 we show six examples of the size-resolved composition of different aerosol samples in two
471 locations (South East England and North Alaska). We can see that the aerosol samples are very
472 different depending on the location. The aerosol samples collected in the UK shown in Fig 11a, c and
473 d are very similar to the sample shown in Fig. 10a. In fact the sample in Figure 10a was taken on the
474 same day in a similar location as the sample in Fig 11b and the similarity between the two helps to
475 demonstrate the reproducibility of our technique. Generally, these samples from S.E. England
476 contained carbonaceous aerosol throughout the size distribution, particularly in the fine mode. This
477 is consistent with typical urban influenced aerosol (Seinfeld and Pandis, 2006). There is also a
478 substantial proportion of mineral dust and only a small proportion of Na rich aerosol. In contrast, the
479 samples collected in North Alaska (close or above the Arctic Ocean) generally contained a smaller
480 proportion of carbonaceous particles, but much larger contributions of Na rich aerosol (very likely sea
481 salt particles, since they were collected in a marine environment). The S-rich category was also
482 substantial in the fine mode in Alaska, consistent with some samples collected in other areas of the
483 Arctic (Young et al., 2016), and some samples collected in a similar location (Creamean et al., 2018).
484 Notably, the coarse mode in Alaska, while generally smaller in number than in S.E. England, contained
485 a high proportion of mineral dusts. This is also consistent with other measurements in the Arctic
486 (Creamean et al., 2018; Young et al., 2016).

487

7. Recommendations for aerosol sampling with the Filters system on the FAAM aircraft

489 Based on the calculations in Sect. 2.1 and the experimental findings in the subsequent sections, we
490 suggest keeping the total flow rate (including the flow through the filters measured by the electronics
491 box plus the bypass flow, which can be between 20 and 35 L min^{-1}) above 50 L min^{-1}. Below this range,
492 the sub-isokinetic enhancement of large aerosol particles is above a factor 2, according to the

493   calculations in Sect. 2.2 that can be seen in Fig. 2b. For total flow rates above 65 L min^{-1}, the flow
494   becomes turbulent throughout the line, which associated losses. However, the calculations shown in
495   Fig. 2c indicate that the combination of the isokinetic enhancements and turbulent losses at 80 L min^{-}
496   ^{1} lead to a reasonably representative sampling, but when it reaches 150 L min^{-1}, the position of the
497   D50 drops to 6.5 µm (not shown in the graph) so such a high flow rate would not be appropriate if the
498   user wants to sample coarse aerosol particles. Hence, we recommend an operational upper limit of
499   80 L min^{-1}. For 0.45 µm PTFE filters and the 0.4 µm polycarbonate filters presented in Fig. 4, sampling
500   close to this flow rate range is often achievable by keeping the bypass open, since this increases the
501   total flow rate and brings it closer to the suggested range, as one can see in Fig. 2c. If other filter types
502   are used, the flow rates will be different to those presented here and these flow rates should be taken
503   in consideration when choosing the pore size (or equivalent pore size) in order to avoid dramatic
504   sampling biases.

505   We already mentioned in Sect. 2.3 that we recommend replacing the side displacement pump with a
506   design that would provide a greater pressure drop. In addition, we also recommend that the bypass
507   flow rate is also routinely measured and controlled in order that the flow at the inlet nozzle can be
508   optimised while sampling.

509

510   **8. Conclusions**

511   In this work we have characterised the filter inlet system on board the FAAM BAe-146 research aircraft
512   which is used for the collection of atmospheric aerosol particles for off line analysis. Our primary goal
513   is to use this inlet system for quantification of INP concentrations and size resolved composition
514   measurements, but it could also be used to derive other quantities with other analytical techniques.

515   In order to characterise the inlet system we made use of an electron microscope technique to study
516   the inlet efficiency, by comparing the SEM size distributions with the in situ size distributions
517   measured with underwing optical probes (PCASP-CDP). In spite of the discrepancies and uncertainties,
518   the sub-isokinetic enhancement of large aerosol particles predicted by the calculations in Sect. 2.2
519   was observed in these comparisons. We also experimentally verify that this enhancement is minimised
520   by operating the inlet with the bypass open which maximised the flow rate through the inlet nozzle.
521   In addition, we note that we performed tests with three very different aerosol distributions and the
522   size distribution of the particles on the filters had comparable features and concentrations to those
523   measured by the underwing optical probes. Overall, the inlet tends to enhance the concentration of
524   aerosol in the coarse mode with a peak enhancement at ~10 µm, but when operated with the
525   recommended flow conditions this enhancement is minimised. The inlet efficiency decreases rapidly
526   for sizes above about 20 µm and becomes highly dependent upon the specifics of the sampling such
527   as flow rates and angle of attack. Based on the calculations we recommend that the total flow rates
528   at the nozzle are maintained at between 50 and 80 L min^{-1}, and also that improvements are made to
529   the pump and bypass flow control (see Sect. 2.3).

530   We also established an SEM technique to determine the size resolved composition of the aerosol
531   sample. Each particle can be categorized based on its chemical composition using a custom made
532   classification scheme. Using this technique we showed that the filter system on board of the FAAM
533   BAe-146 spreads the particles evenly across the filter surface, which is necessary for the SEM size
534   distribution analysis.

535   Having a well characterised inlet allows us to sample aerosol particles up to around 20 µm with
536   knowledge of the likely biases from the aircraft. Hence, we can use this inlet system to collect aerosol

537   for offline analysis at altitudes which are relevant for clouds. For example, this may allow us to use the
538   size resolved aerosol composition to quantify the size distribution of individual aerosol components
539   at a particular location and combine this information with INP measurements to quantify the surface
540   area normalised ice nucleating ability of a specific class of aerosol.

541

542 **Appendix A: discussion of the inlet efficiency calculations**

543 Here we include a further description of the efficiency mechanisms used in the inlet model described
544 in Fig. 2 and discuss the choice of the equations and their limits of validity:

545 *Aspiration efficiency* accounts for the fact that the speed of the sampled air mass (U_0), and the speed
546 of the air through the beginning of the nozzle (U) are different. When these two speeds are equal, the
547 sampling is called "isokinetic", whereas when the speeds don't match, the sampling is called super
548 isokinetic or sub-isokinetic depending on if U_0 is smaller or larger than U respectively. In our case, the
549 air mass moves at the flying speed, which varies with the altitude (110 m s^{-1} is a typical value for
550 sampling altitudes), and the speed at the start of the inlet is almost always below 35 m s^{-1} (sub-
551 isokinetic conditions). As a consequence, some air streamlines will be forced around the inlet, while
552 high inertia particles won't, which will lead to an aspiration efficiency above 1 for coarse mode aerosol
553 particles. This enhancement is greater for large particles due to their large inertia which makes difficult
554 their ability to follow the air streamlines. The enhancement reaches a maximum value of U_0/U in its
555 high diameter limit (when none of the particles in the sampled air mass follow the streamlines that
556 escape from the inlet and all of them are sampled). The aspiration efficiency tends to 1 (no
557 enhancement) for small diameters.

558 This behaviour has been characterised by several studies (we will only look at the sub-isokinetic range
559 of the equations since it is impossible to reach the super isokinetic range during flight). An empirical
560 equation was developed based on laboratory experiment by Belyaev and Levin (1972) and Belyaev
561 and Levin (1974) (referred as B&L) for certain range of U/ U_0 ratio and Stokes number. However, for
562 ratios below its experimental range (U/ U_0>0.2), the B&L function doesn't make physical sense since
563 it converges to values above 1 for small particle sizes. The aircraft inlet system works at smaller U/ U_0
564 ratios sometimes, so this function is not very accurate to describe the behaviour of the system in such
565 conditions. Liu et al. (1989) developed another function (referred as LZK) by means of a numerical
566 simulation based on computational fluid mechanics. The U/ U_0 ratio and Stokes number valid range is
567 wider than the B&L expression (down to 0.1). It agrees with the B&L expression in the U/ U_0 ratio the
568 latter was developed for. For smaller values of the ratio, the LZK function are believed to be more
569 accurate, since it predicts the known physical behaviour (no sub-isokinetic enhancement for small
570 particle sizes). It reaches U/ U_0 ratios down to 0.2, which is enough to cover most of the total flow
571 rates achieved in the inlet system. (Krämer and Afchine, 2004) developed another expression (referred
572 as K&A) for 0.007< U/ U_0<0.2 based on computational fluid dynamics. However, for low particle sizes,
573 the efficiency doesn't converge to 1. As a consequence, we have used the LZK (Liu et al., 1989) function
574 since it covers most of the U/ U_0 ratios we get in the inlet system, it agrees with the experimental data
575 in Belyaev and Levin (1972) and Belyaev and Levin (1974) and it converges to U_0/U for large particles
576 sizes and 1 for small particle sizes. Outside its valid range (U / U_0 < 0.1), the LZK function agrees with
577 the K&A function for large radius and converges to 1 for small particle sizes. The equation is valid for
578 0.01<Stks<100, which is enough to cover the range in between 1 and 100 μm. As already stated, it
579 tends to 1 for small particles sizes and to U_0/U for large particles sizes (At 50 L min^{-1}, the ratio U/U_0 is
580 0.2). All the calculations were done under standard conditions (0 °C and 1 bar). The effect of changes
581 in pressure and temperature (and therefore air density and dynamic viscosity) that normally occur in
582 the filter inlet system sampling range (0 to 3000 m), are negligible in all the used equations as shown
583 in Fig. S1 in the supplementary information.

584 The used equations (as well as the ones used for anisoaxial losses) have been developed for thin-
585 walled nozzles, (this criteria was defined first in Belyaev and Levin (1974)). The inlet has been
586 described as thin-walled in the literature (Andreae et al., 2000; Formenti et al., 2003; Talbot et al.,
587 1990) but we haven't used this terminology here since it is not possible to numerically quantify this

588 using the criteria given in (Belyaev and Levin, 1974) because the edge of the nozzle is curved. However,
589 the inlet has been designed to avoid distortion of the pressure field at the nozzle tip and the resulting
590 problems associated with flow separation and turbulence (Andreae et al., 1988) which is the main
591 caveat of inlet nozzles that are not thin-walled (Belyaev and Levin, 1974). As a consequence, we used
592 these sets of equations for thin-walled nozzles to describe the filter inlet system considered in this
593 study. The fact that the calculations done using this equations show that the filter inlet system has
594 biases with similar characteristics as the ones estimated experimentally for coarse aerosol particles
595 helps to support this assumption.

596 *Inlet inertial deposition i*s defined as the inertial loss of aerosol particles when they enter nozzle. It is
597 produced by the fact that the streamlines bend towards the walls at the moment they enter the
598 nozzle, some large inertia particles can impact the walls and get deposited. Here, we have used the
599 equation given in Liu et al. (1989) which quantifies this effect. It is also valid for 0.01<Stks<100, which
600 is enough to cover the range in between 1 and 100 μm.

601 *Turbulent inertial deposition* happens when some particles are collected by the wall when travelling
602 in a pipe in the turbulent regime because some of the particles cannot follow the eddies of the
603 turbulent flow. In order to include this mechanism, we used the equation given in Brockmann (2011),
604 using the relation in between the deposition velocity and dimensionless particle relaxation time given
605 by Liu and Ilori (1974). These calculations are valid for a cylindrical pipe, whereas the turbulent section
606 of the inlet considered here is the nozzle, which has a conical shape. In order to account for this, we
607 divided the conical nozzle into 90 conical sections with an increasing diameter and a length of 1mm,
608 and combined the effect of all the sections. This approach does not account for the additional inertial
609 losses that could occur as a consequence of turbulence created by the enlargement of the flow in the
610 conical section. However, the angle of enlargement is small (5.7°). It was designed to be below 7° in
611 order to avoid flow separation (Andreae et al., 1988). As already mentioned, above 65 L min^{-1},
612 turbulent flow occurs in the whole inlet tube. This has been taken into account in the 80 L min^{-1} case
613 in Fig. 2b. The equation used here has been tested for size ranges in between 1.4 and 20 μm, and
614 doesn't depend on the Reynolds number values it was tested for (10000 and 50000) (Liu and Ilori,
615 1974).

616 *Bending inertial deposition* was also considered, since the line curves with an angle of 45° in order to
617 bring the airstream into the cabin. The inertia of some particles may keep them in their original track
618 and they are not able to follow the air streamlines that are bending towards the cabin, following the
619 inlet tubes. In order to account for these losses, we have used the empirical equation given in
620 Brockmann (2011) based on the data from Pui et al. (1987) for laminar flow. This equation was
621 developed for Reynold numbers of 1000, and we have used it for higher values. However, in
622 Brockmann (2011), one can see that the data from Pui et al. (1987) for Re=6000 (beginning of the
623 turbulent flow regime) doesn't differ that much from the fit we have used (valid for Re=1000). Since
624 our Re numbers for the thick section of the tube almost never go above 5000, we can still use the
625 laminar flow fit. This model has been tested for 0.08 < Stks < 1.2, which is enough to cover most of the
626 range where the inertial deposition efficiency drops from 1 to 0. The main caveat of this calculation is
627 that the model considers a smooth tube where that the flow rate before and after the bending is the
628 same, while in the inlet system, if the bypass flow is on, the flow rate before and after the bending is
629 different (before it, it would be equal to the total flow rate, whereas after the bending, it would be
630 equal to the filter flow rate). As a consequence we assumed that the flow rate after the bending is
631 equal to the total flow rate. This assumption might underestimate the losses since some large aerosol
632 particles will become accumulated in the bypass.

633 *Gravitational settling* was also considered. We used the analytical equation given by Thomas (1958),
634 as stated in Brockmann (2011). We applied this equation for the section of the pipe from the nozzle
635 to the bend (15 cm long). We used the modification (also analytical) of the previous equation given in
636 Heyder and Gebhart (1977) in order to account for the losses in the second section of the tube which
637 is 40 cm long and it is bended 45°. The gravitational losses in the nozzle were neglected since the
638 settling distance is much shorter and the time the air takes to pass it is smaller since it travels quicker.
639 As stated previously, the lower part of the turbulent regime can be reached for high flow rates through
640 all the tube. For these cases, we still use this equation which is only valid for the laminar regime, since
641 the gravitational settling efficiencies for the turbulent regime are very close to the laminar regime
642 ones (Brockmann, 2011) and wouldn't make a significant difference in our calculations.

643 *Diffusional efficiency* accounts for the fact that small aerosol particles could diffuse to the walls of the
644 pipe via Brownian motion. In order to account for this phenomenon, we have used the analytic
645 equation by Gormley and Kennedy (1948) as stated in Brockmann (2011). We have assumed that
646 diffusion happens only in the tube (before and after the bend) and excluding the diffusion in the nozzle
647 since it is negligible because these losses are a function of the residence time and the residence time
648 of the aerosol particles in the nozzle is much smaller than the rest of the tube. F or this calculation,
649 we have assumed 0 °C and 1 atm. We didn't show the efficiency associated to diffusion in Fig. 2a
650 because it was very close to 1 for all considered sizes. It only becomes slightly smaller than 1 for sizes
651 below 20 nm at 50 L min^{-1}. As a consequence, the inlet could be potentially used to sample nucleation
652 mode aerosol particles, even though for this study we will only focus on the particles larger than 0.1
653 μm.

654 *Filter collection efficiency* accounts for the fact that some particles can pass through the pores of the
655 filter, if they are smaller than the pores. However, filter pore size (in the case of polycarbonate
656 capillarity filters) and filter equivalent pore size (in the case of PTFE porous filters) is sometimes
657 misunderstood as a size cut off at which smaller particles are lost and larger particles are captured.
658 However, particle collection on filters happens through several mechanisms including interception,
659 impaction, diffusion, gravitational settling or by electrostatic attraction under certain conditions
660 (Flagan and Seinfeld, 1988; Lee and Ramamurthi, 1993). As a consequence, particles with diameters
661 below the pore size are normally collected (Lindsley, 2016; Soo et al., 2016). 99.48% of the generated
662 sodium chloride particles with sizes in between 10.4 and 412 nm were collected by a 0.4 μm
663 polycarbonate filter at flow rates below 11.2 L min^{-1} (smaller than most of the flow rates at which the
664 air passes through the same filters in the FAAM filter inlet system) (Soo et al., 2016). As a consequence,
665 we assumed a filter collection efficiency of 100% across the whole considered size range (0.1 to 100
666 μm). However, the fact that some aerosol particles with diameters below the pore size could be
667 deposited in the filter pores and therefore not be detected by the SEM technique could contribute to
668 the undercounting.

669 *Anisoaxial losses* have not been considered in the analysis shown in Fig. 2, after estimating that they
670 would only affect particles significantly larger than 10 μm and the fact that the alignment of the inlet
671 is difficult to quantify and the angle of attack changes during the flight. Using the equations explained
672 in Hangal and Willeke (1990a), we calculated that the modification of the sub-isokinetic behaviour of
673 the inlet produced by small values of θ is negligible. The equation was used beyond its experimental
674 limit, but this extrapolation was justified by the fact that the equation for θ = 0 made asymptotic
675 physical sense at the low and high Stokes number limits and produced very similar results to the ones
676 showed in Fig. 2a. Anisoaxial sampling can also produce inertial losses when particles impact the walls
677 of the inlet. These ones have been quantified using the expression given by Hangal and Willeke
678 (1990b) for different values of θ and they can be seen in Fig. 3. This mechanism looks very similar to

679 the gravitational and bend deposition efficiency shown in Fig. 2a. Anisoaxial inertial losses add a cut
680 off that prevents large particles to be sampled. As one can see in Fig. 3, the effect is very dependent
681 on the angle and only affects particles significantly larger than 10 µm in most cases, so it hasn't been
682 included in the total analysis shown in the Fig 2. One can see in Fig. 3 that the position of the D50 of
683 the anisoaxial cut off decreases when increasing values of θ up to 2°. For values of θ between 2° and
684 6°, it increases when increasing θ.

685 *Other losses:* Some mechanisms (thermophoresis, diffusiophoresis, interception, coagulation and re-
686 entrainment of deposited particles) have not been considered, since they are second order
687 mechanisms under our conditions when compared with the calculated mechanisms (Brockmann,
688 2011; von der Weiden et al., 2009) and for one of them (electrostatic deposition) it is not possible to
689 quantify them. Electrostatic deposition is normally avoided by using grounded conductive materials
690 so no electrical field exists within the tubing (Brockmann, 2011). Since the FAAM BAe-146 research
691 aircraft is not grounded during the flight, we cannot state this mechanism is irrelevant. However, the
692 experimental agreement between the SEM and optical probes suggest that this is a minor loss
693 mechanism.

694

695 **Appendix B. SEM compositional categories**

696 Here we describe the 10 categories we have used in our compositional analysis, which are a summary
697 of the 32 rules described in the supplementary information. The approach has some similarities with
698 the ones in previous studies (Chou et al., 2008; Hand et al., 2010; Kandler et al., 2011; Krejci et al.,
699 2005; Young et al., 2016), but it is distinct. Because of the fact that the filter is made of C and O,
700 background elements (C and O) were detected in all the particles. Particles in each category can
701 contain smaller amounts of other elements apart from the specified ones. This classification scheme
702 has been designed a posteriori to categorise the vast majority of the aerosol particles in the three field
703 campaigns previously described and some ground collected samples in the UK and Barbados. The main
704 limitation of the classification scheme is the difficulty to categorise internally mixed particles. The
705 algorithm has been built in a way it can identify mixtures of mineral dust and sodium chloride (they
706 appear as mineral dust but they could be split into a different category if necessary) and sulphate or
707 nitrate ageing on sodium chloride (they appear as Na rich but it could also be split into a different
708 category). However, other mixtures of aerosol wouldn't be identified, and they would be categorised
709 by the main component in the internal mixture in most cases.

710 B.1. Carbonaceous

711 The particles in this category contained only background elements (C and O). The components of the
712 carbonaceous particles consist in either black carbon from combustion processes or organic material,
713 which can be either directly emitted from sources or produced by atmospheric reactions (Seinfeld and
714 Pandis, 2006). Particles containing certain amount of K and P in addition to the background elements
715 were also accepted in these category. These elements are consistent with biogenic origin aerosol
716 particles (Artaxo and Hansson, 1995). Distinction between organic and black carbon aerosol
717 unfortunately could not reliably be done. Since N is not analysed in our SEM set up, any nitrate aerosol
718 particle would fall into this category if it is on the filter. However, since these particles are semi-
719 volatile, some of these aerosol particles would not resist the low pressure of the SEM chamber. This
720 could be further investigated in the future.

721 B.2. S rich

722 Aerosol particles in this category contained a substantial amount of S. This S might be in the form of
723 inorganic or organic sulphate compounds. Some sulphate compounds, such as sulphuric acid, are
724 relatively volatile and will be lost in the SEM chamber.

725 B.3 Metal rich

726 The composition of particles in this category is dominated by one of the following metals: Fe, Cu, Pb,
727 Al, Ti, Zn or Mn. These EDS signatures are compatible with metallic oxides or other metal rich particles.
728 These metal containing particles can originate from both natural sources and anthropogenic sources.
729 Some metallic oxides are common crustal materials that could go into the atmosphere but are also
730 produced during some combustion processes (Seinfeld and Pandis, 2006). In addition, many types of
731 metal and metallic derivatives particles are produced as component of industrial emissions and other
732 anthropogenic activities (Buckle et al., 1986), (Fomba et al., 2015).

733 B.4. Na rich

734 Sodium chloride particles are the main component of the sea spray aerosol particles which are emitted
735 through wave breaking processes (Cochran et al., 2017). These particles can age in the atmosphere by
736 reacting with atmospheric components such as sulphuric or nitric acid (Graedel and Keene, 1995),
737 (Seinfeld and Pandis, 2006). As a consequence of this reaction, a part of their Cl content will end up in
738 the gaseous phase (as HCl), leading to an apparent chlorine deficit in the aged sea spray aerosol
739 particles. Particles in this category have an EDS signature compatible with sea spray aerosol particles
740 since they are identified by the presence of Na, containing in most cases Cl and/or S (N is not included
741 in our SEM analysis).

742 B.5 Cl rich

743 Particles in this category contained mainly Cl and sometimes also K but never Na, so they are not
744 sodium chlorine particles. Significant concentrations of Cl and metals in aerosol particles have been
745 linked to industrial activities, coal combustion, incineration and automobile emissions (Graedel and
746 Keene, 1995; Paciga et al., 1975), whereas Cl and K in aerosol particles could be originated by the use
747 of fertilisers (Angyal et al., 2010), biomass burning (Lieke et al., 2017; Zender et al., 2003), or emitted
748 during pyrotechnic events (Crespo et al., 2012).

749 B.6 Ca rich

750 The composition of the particles in this category is dominated by Ca. In this category, particles
751 containing only Ca (plus C and O, the background elements) are consistent with calcium carbonate, a
752 major component of mineral dust (Gibson et al., 2006). If other elements such as Mg and S are present,
753 the signature of the particles compatible with some mineral origin elements as gypsum and dolomite
754 respectively. In addition, presence of minor amounts of Si, Al and other elements could indicate mixing
755 of these Ca rich particles with some other soil components as silicates. However, since Ca is a biogenic
756 element, we cannot discard the biogenic origin of some of the Ca-rich particles (Krejci et al., 2005).
757 Some Ca rich particles could originate from the crystallization of sea water, loosely attached to NaCl.
758 The latter component would dominate over the rest of the elements of the conglomerate and they
759 would appear as Na rich particles, unless they shatter in the air (Hoornaert et al., 1996; Parungo et al.,
760 1986).

761

762 B.7 Al-Si rich

763 Particles in the Al-Si rich category were detected by the presence of Al and Si as major elements. Very
764 often, this particles also contained smaller amounts of Na, Mg, K, Ca, Ti, Mn and Fe. Particles in this
765 category are very likely to have mineral origin and are commonly described as aluminosilicates which
766 include a range of silicates such as feldspars and clays (Chou et al., 2008; Hand et al., 2010). Mixed
767 mineral origin particles containing both Al and Si can also fall into this category. Strong presence of Na
768 and Cl could indicate internal mixing with some sea spray aerosol, whereas a strong S presence could
769 indicate atmospheric acid ageing.

770 B.8 Si only

771 The particles in this category contained only Si apart from the background elements. Particles in this
772 category are very likely to be a silica polymorph (mainly quartz), one of the major components of the
773 earth's crust. Since we cannot determine if the C signal in the EDS of these particles is produced from
774 the background or from the particle itself, a particle containing only C, Si and O would fall into this
775 category, however, mineral phases containing these elements are extremely rare.

776 B.9 Si rich

777 The composition of these particles was dominated by Si, and other elements Na, Mg, K, Ca, Ti, Mn and
778 Fe. The main difference with the particles in B7 is that the ones described here didn't contain Al above
779 the limit of detection. The EDS signal of particles in this category is compatible with any silicate that
780 does not contain Al as a major component in its phase such as talc or olivine. The only exception is
781 quartz, which falls in the 'Si only' category described above. They could also be internal mixtures of
782 silica or silicates without aluminium as a major component in its phase. Because of the high limit of
783 detection of the Al (See the SI), some particles in this category could contain small amounts of Al, and
784 should belong to Al-Si rich category. As in the Al-Si rich particles case, strong presence of Na and Cl
785 could indicate internal mixing with some sea spray aerosol, whereas a strong S presence could indicate
786 atmospheric acid ageing.

787 Some of these categories could be further grouped. For example, the particles in the Ca rich, Al-Si
788 rich, Si only and Si rich categories could be considered as "mineral dust". However, if the sample
789 contains ash from combustion processes or volcanic origin, it will also appear in these last categories
790 since its composition is similar to mineral dust (Chen et al., 2012; Nakagawa and Ohba, 2003).

791

Appendix C. Weight percentage confidence level sensitivity test

The software calculates the weight percentage (wt %) of each detected element with its statistical error (σ). In our classification scheme, we have imposed the rule that all the detected elements must be statistically significant in order to be considered as present (the wt % of each detected element needs to be a certain confidence level above the σ. We explored the appropriate value of sigma for our application below.

Our analysis is distinguished from others in the literature in that we use a relatively thick Ir coating (30 nm) as well as a relatively low EDS integration time in order to get data from many particles in a session. Some of the secondary EDS peaks of Ir overlap in some cases with some of the atmospherically relevant elements (the primary peak does not). This produces some issues like a larger σ in some elements. This effect is quite noticeable for Al and S, where some clear peaks of these elements were not statistically significant at a confidence level of 3. In Fig. C1 we show the results of a test where we studied the effect of changing the confidence level from 3 to 2 σ in the particle categorisation carried out by the classification scheme. The only effect of this change yields on the Al and S. When going from 3 to 2 σ as a confidence level, more Al is detected in the sample, so some Si-rich particles (from rule 25) are detected as Al-Si rich particles (rule 5) instead. Manual inspection of a subset of these particles revealed that the Al peak that wasn't being identified at 3 σ is an actual Al signal that was detected at 2 σ. Likewise, some significant S peaks were not being detected at a confidence level of 3 σ but they were at 2 σ, leading to more S rich particles (rule 14) that were labelled as Other from the rule 32 at a higher confidence level. The variation in the confidence level didn't modify the number of particles in other categories, so we recommend the use a 2 σ value in order to minimise the underestimation of Al-Si and S rich particles.

Acknowledgements

We a grateful for helpful discussions with Paola Formenti (Centre National de la Recherche Scientifique), Hannah Price (FAAM) and Eduardo Morgado (School of Earth and Environment, University of Leeds). Airborne data were obtained using the FAAM BAe-146-301 Atmospheric Research Aircraft, flown by Airtask Ltd and managed by FAAM Airborne Laboratory, jointly operated by UKRI and the University of Leeds. We thank all the people involved in the EMERGE, VANAHEIM and MACSSIMIZE campaigns, as well as Avalon. We acknowledge the Leeds Electron Microscopy and Spectroscopy Centre for the use of their microscopy facilities and the Centre for Environmental Data Analysis for providing us with the FAAM datasets used here. We are grateful for funding from the European Research Council (ERC) (648661 MarineIce).

Data availability

Data presented in this paper is available at: https://doi.org/10.5518/724. Unprocessed PCASP-CDP data can be found in the FAAM cloud datasets corresponding to each flight at the Centre for Environmental Data Analysis.

832 **References**

833 Albrecht, B. A.: Aerosols, cloud microphysics, and fractional cloudiness, Science, 245, 1227-1230, 1989.
834 Andreae, M. O., Berresheim, H., Andreae, T. W., Kritz, M. A., Bates, T. S., and Merrill, J. T.: Vertical-
835 Distribution of Dimethylsulfide, Sulfur-Dioxide, Aerosol Ions, and Radon over the Northeast Pacific-
836 Ocean, J. Atmos. Chem., 6, 149-173, 1988.
837 Andreae, M. O., Elbert, W., Gabriel, R., Johnson, D. W., Osborne, S., and Wood, R.: Soluble ion
838 chemistry of the atmospheric aerosol and SO2 concentrations over the eastern North Atlantic during
839 ACE-2, Tellus B, 52, 1066-1087, 2000.
840 Angyal, A., Kertész, Z., Szikszai, Z., and Szoboszlai, Z.: Study of Cl-containing urban aerosol particles by
841 ion beam analytical methods, Nucl. Instrum. Methods Phys. Res. B, 268, 2211-2215, 2010.
842 Artaxo, P. and Hansson, H. C.: Size Distribution of Biogenic Aerosol-Particles from the Amazon Basin,
843 Atmos. Environ., 29, 393-402, 1995.
844 Baumgardner, D., Brenguier, J. L., Bucholtz, A., Coe, H., DeMott, P., Garrett, T. J., Gayet, J. F., Hermann,
845 M., Heymsfield, A., Korolev, A., Kramer, M., Petzold, A., Strapp, W., Pilewskie, P., Taylor, J., Twohy, C.,
846 Wendisch, M., Bachalo, W., and Chuang, P.: Airborne instruments to measure atmospheric aerosol
847 particles, clouds and radiation: A cook's tour of mature and emerging technology, AtmRe, 102, 10-29,
848 2011.
849 Baumgardner, D. and Huebert, B.: The airborne aerosol inlet workshop: Meeting report, J. Aerosol Sci,
850 24, 835-846, 1993.
851 Belyaev, S. P. and Levin, L. M.: Investigation of aerosol aspiration by photographing particle tracks
852 under flash illumination, J. Aerosol Sci, 3, 127-140, 1972.
853 Belyaev, S. P. and Levin, L. M.: Techniques for collection of representative aerosol samples, J. Aerosol
854 Sci, 5, 325-338, 1974.
855 Bergin, M. H., Ogren, J. A., Schwartz, S. E., and McInnes, L. M.: Evaporation of ammonium nitrate
856 aerosol in a heated nephelometer: Implications for field measurements, Environ. Sci. Technol., 31,
857 2878-2883, 1997.
858 Brockmann, J. E.: Aerosol Transport in Sampling Lines and Inlets. In: Aerosol Measurement, John Wiley
859 & Sons, Inc., 2011.
860 Buckle, R., Tsakiropoulos, P., and C. Pointon, K.: Preparation and properties of metallic aerosol
861 particles, Int. Mater. Rev., 31, 258-288, 1986.
862 Chen, H., Laskin, A., Baltrusaitis, J., Gorski, C. A., Scherer, M. M., and Grassian, V. H.: Coal fly ash as a
863 source of iron in atmospheric dust, Environ. Sci. Technol., 46, 2112-2120, 2012.
864 Chou, C., Formenti, P., Maille, M., Ausset, P., Helas, G., Harrison, M., and Osborne, S.: Size distribution,
865 shape, and composition of mineral dust aerosols collected during the African Monsoon
866 Multidisciplinary Analysis Special Observation Period 0: Dust and Biomass-Burning Experiment field
867 campaign in Niger, January 2006, J. Geophys. Res. Atmos., 113, 1-17, 2008.
868 Cochran, R. E., Ryder, O. S., Grassian, V. H., and Prather, K. A.: Sea Spray Aerosol: The Chemical Link
869 between the Oceans, Atmosphere, and Climate, Acc. Chem. Res., 50, 599-604, 2017.
870 Creamean, J. M., Kirpes, R. M., Pratt, K. A., Spada, N. J., Maahn, M., de Boer, G., Schnell, R. C., and
871 China, S.: Marine and terrestrial influences on ice nucleating particles during continuous springtime
872 measurements in an Arctic oilfield location, Atmos. Chem. Phys, 18, 18023-18042, 2018.
873 Crespo, J., Yubero, E., Nicolas, J. F., Lucarelli, F., Nava, S., Chiari, M., and Calzolai, G.: High-time
874 resolution and size-segregated elemental composition in high-intensity pyrotechnic exposures, J.
875 Hazard. Mater., 241-242, 82-91, 2012.
876 DeMott, P. J., Prenni, A. J., Liu, X., Kreidenweis, S. M., Petters, M. D., Twohy, C. H., Richardson, M. S.,
877 Eidhammer, T., and Rogers, D. C.: Predicting global atmospheric ice nuclei distributions and their
878 impacts on climate, Proc Natl Acad Sci U S A, 107, 11217-11222, 2010.
879 Egerton, R. F.: Physical principles of electron microscopy, Springer US, 2005.
880 Flagan, R. C. and Seinfeld, J. H.: Removal of particles from gas streams. In: Fundamentals of Air
881 Pollution Engineering, Prentice-Hall, Inc., Englewood Cliffs, NJ, 1988.

Fomba, K. W., van Pinxteren, D., Muller, K., Iinuma, Y., Lee, T., Collett, J. L., and Herrmann, H.: Trace metal characterization of aerosol particles and cloud water during HCCT 2010, Atmos. Chem. Phys, 15, 8751-8765, 2015.

Formenti, P., Elbert, W., Maenhaut, W., Haywood, J., and Andreae, M. O.: Chemical composition of mineral dust aerosol during the Saharan Dust Experiment (SHADE) airborne campaign in the Cape Verde region, September 2000, J. Geophys. Res., 108, 8576, 2003.

Gao, Y., Anderson, J. R., and Hua, X.: Dust characteristics over the North Pacific observed through shipboard measurements during the ACE-Asia experiment, Atmos. Environ., 41, 7907-7922, 2007.

Gibson, E. R., Hudson, P. K., and Grassian, V. H.: Aerosol chemistry and climate: Laboratory studies of the carbonate component of mineral dust and its reaction products, Geophys Res Lett, 33, 1-5, 2006.

Gormley, P. G. and Kennedy, M.: Diffusion from a Stream Flowing through a Cylindrical Tube, Math. Proc. Royal Ir. Acad., 52, 163-169, 1948.

Graedel, T. E. and Keene, W. C.: Tropospheric budget of reactive chlorine, Global Biogeochem. Cycles, 9, 47-77, 1995.

Hamacher-Barth, E., Jansson, K., and Leck, C.: A method for sizing submicrometer particles in air collected on Formvar films and imaged by scanning electron microscope, Atmos. Meas. Tech., 6, 3459-3475, 2013.

Hand, V. L., Capes, G., Vaughan, D. J., Formenti, P., Haywood, J. M., and Coe, H.: Evidence of internal mixing of African dust and biomass burning particles by individual particle analysis using electron beam techniques, J. Geophys. Res., 115, 1-11, 2010.

Hangal, S. and Willeke, K.: Aspiration efficiency: unified model for all forward sampling angles, Environ. Sci. Technol., 24, 688-691, 1990a.

Hangal, S. and Willeke, K.: Overall Efficiency of Tubular Inlets Sampling at 0-90 Degrees from Horizontal Aerosol Flows, Atmos Environ a-Gen, 24, 2379-2386, 1990b.

Haywood, J. and Boucher, O.: Estimates of the direct and indirect radiative forcing due to tropospheric aerosols: A review, Rev Geophys, 38, 513-543, 2000.

Heyder, J. and Gebhart, J.: Gravitational deposition of particles from laminar aerosol flow through inclined circular tubes, J. Aerosol Sci, 8, 289-295, 1977.

Hoornaert, S., Van Malderen, H., and Van Grieken, R.: Gypsum and Other Calcium-Rich Aerosol Particles above the North Sea, Environ. Sci. Technol., 30, 1515-1520, 1996.

Hoose, C. and Mohler, O.: Heterogeneous ice nucleation on atmospheric aerosols: a review of results from laboratory experiments, Atmos. Chem. Phys, 12, 9817-9854, 2012.

Hyuk Kim, C.: Characterization of Volatilization of Filter-Sampled PM2.5 Semi-Volatile Inorganic Ions Using a Backup Filter and Denuders, Aerosol Air Qual. Res., 2015, 2015.

Kandler, K., Benker, N., Bundke, U., Cuevas, E., Ebert, M., Knippertz, P., Rodríguez, S., Schütz, L., and Weinbruch, S.: Chemical composition and complex refractive index of Saharan Mineral Dust at Izaña, Tenerife (Spain) derived by electron microscopy, Atmos. Environ., 41, 8058-8074, 2007.

Kandler, K., Lieke, K., Benker, N., Emmel, C., Kupper, M., Muller-Ebert, D., Ebert, M., Scheuvens, D., Schladitz, A., Schutz, L., and Weinbruch, S.: Electron microscopy of particles collected at Praia, Cape Verde, during the Saharan Mineral Dust Experiment: particle chemistry, shape, mixing state and complex refractive index, Tellus B, 63, 475-496, 2011.

Kandler, K., Schneiders, K., Ebert, M., Hartmann, M., Weinbruch, S., Prass, M., and Pohlker, C.: Composition and mixing state of atmospheric aerosols determined by electron microscopy: method development and application to aged Saharan dust deposition in the Caribbean boundary layer, Atmos. Chem. Phys, 18, 13429-13455, 2018.

Kim, J., Bauer, H., Dobovicnik, T., Hitzenberger, R., Lottin, D., Ferry, D., and Petzold, A.: Assessing Optical Properties and Refractive Index of Combustion Aerosol Particles Through Combined Experimental and Modeling Studies, Aerosol Sci. Technol., 49, 340-350, 2015.

Krämer, M. and Afchine, A.: Sampling characteristics of inlets operated at low U/U0 ratios: new insights from computational fluid dynamics (CFX) modeling, J. Aerosol Sci, 35, 683-694, 2004.

932 Krejci, R., Strom, J., de Reus, M., and Sahle, W.: Single particle analysis of the accumulation mode
933 aerosol over the northeast Amazonian tropical rain forest, Surinam, South America, Atmos. Chem.
934 Phys, 5, 3331-3344, 2005.
935 Laskin, A. and Cowin, J. P.: Automated single-particle SEM/EDX analysis of submicrometer particles
936 down to 0.1 μm, Anal Chem, 73, 1023-1029, 2001.
937 Lee, K. W. and Ramamurthi, M.: Chapter 10: Filter Collection. In: Aerosol Measurement: Principles,
938 Techniques, and Applications

939 Willeke, K. and Baron, P. (Eds.), Van Nostrand Reinhold, New York, 1993.
940 Lieke, K., Kandler, K., Scheuvens, D., Emmel, C., Glahn, C. V., Petzold, A., Weinzierl, B., Veira, A., Ebert,
941 M., Weinbruch, S., and Schütz, L.: Particle chemical properties in the vertical column based on aircraft
942 observations in the vicinity of Cape Verde Islands, Tellus B: Chemical and Physical Meteorology, 63,
943 497-511, 2017.
944 Lindsley, W. G.: Filter Pore Size and Aerosol Sample Collection, NIOSH Manual of Analytical Methods,
945 2016. 1-14, 2016.
946 Liu, B. Y. H. and Ilori, T. A.: Aerosol deposition in turbulent pipe flow, Environ. Sci. Technol., 8, 351-
947 356, 1974.
948 Liu, B. Y. H., Zhang, Z. Q., and Kuehn, T. H.: A Numerical Study of Inertial Errors in Anisokinetic
949 Sampling, J. Aerosol Sci, 20, 367-380, 1989.
950 Lohmann, U. and Diehl, K.: Sensitivity Studies of the Importance of Dust Ice Nuclei for the Indirect
951 Aerosol Effect on Stratiform Mixed-Phase Clouds, J. Atmospheric Sci., 63, 968-982, 2006.
952 Lohmann, U. and Gasparini, B.: A cirrus cloud climate dial?, Science, 357, 248-249, 2017.
953 Mason, R. H., Si, M., Chou, C., Irish, V. E., Dickie, R., Elizondo, P., Wong, R., Brintnell, M., Elsasser, M.,
954 Lassar, W. M., Pierce, K. M., Leaitch, W. R., MacDonald, A. M., Platt, A., Toom-Sauntry, D., Sarda-
955 Esteve, R., Schiller, C. L., Suski, K. J., Hill, T. C. J., Abbatt, J. P. D., Huffman, J. A., DeMott, P. J., and
956 Bertram, A. K.: Size-resolved measurements of ice-nucleating particles at six locations in North
957 America and one in Europe, Atmos. Chem. Phys, 16, 1637-1651, 2016.
958 McConnell, C. L., Formenti, P., Highwood, E. J., and Harrison, M. A. J.: Using aircraft measurements to
959 determine the refractive index of Saharan dust during the DODO Experiments, Atmos. Chem. Phys,
960 10, 3081-3098, 2010.
961 McMurry, P.: A review of atmospheric aerosol measurements, Atmos. Environ., 34, 1959-1999, 2000.
962 Nakagawa, M. and Ohba, T.: Minerals in Volcanic Ash 1: Primary Minerals and Volcanic Glass, Global
963 Environ. Res., 6, 2003.
964 Nessler, R., Bukowiecki, N., Henning, S., Weingartner, E., Calpini, B., and Baltensperger, U.:
965 Simultaneous dry and ambient measurements of aerosol size distributions at the Jungfraujoch, Tellus
966 B, 55, 808-819, 2003.
967 Paciga, J. J., Roberts, T. M., and Jervis, R. E.: Particle-Size Distributions of Lead, Bromine, and Chlorine
968 in Urban-Industrial Aerosols, Environ. Sci. Technol., 9, 1141-1144, 1975.
969 Parungo, F. P., Nagamoto, C. T., and Harris, J. M.: Temporal and spatial variations of marine aerosols
970 over the Atlantic Ocean, AtmRe, 20, 23-37, 1986.
971 Price, H. C., Baustian, K. J., McQuaid, J. B., Blyth, A., Bower, K. N., Choularton, T., Cotton, R. J., Cui, Z.,
972 Field, P. R., Gallagher, M., Hawker, R., Merrington, A., Miltenberger, A., Neely Iii, R. R., Parker, S. T.,
973 Rosenberg, P. D., Taylor, J. W., Trembath, J., Vergara-Temprado, J., Whale, T. F., Wilson, T. W., Young,
974 G., and Murray, B. J.: Atmospheric Ice-Nucleating Particles in the Dusty Tropical Atlantic, J. Geophys.
975 Res. Atmos., 123, 2175-2193, 2018.
976 Pruppacher, H. R. and Klett, J. D.: Microphysics of Clouds and Precipitation Dordrecht: Kluwer
977 Academic Publishers, 1997.
978 Pui, D. Y. H., Romay-Novas, F., and Liu, B. Y. H.: Experimental Study of Particle Deposition in Bends of
979 Circular Cross Section, Aerosol Sci. Technol., 7, 301-315, 1987.
980 Reid, E. A., Reid, J. S., Meier, M. M., Dunlap, M. R., Cliff, S. S., Broumas, A., Perry, K., and Maring, H.:
981 Characterization of African dust transported to Puerto Rico by individual particle and size segregated
982 bulk analysis, J. Geophys. Res. Atmos., 108, -, 2003.

Rosenberg, P. D., Dean, A. R., Williams, P. I., Dorsey, J. R., Minikin, A., Pickering, M. A., and Petzold, A.: Particle sizing calibration with refractive index correction for light scattering optical particle counters and impacts upon PCASP and CDP data collected during the Fennec campaign, Atmos. Meas. Tech., 5, 1147-1163, 2012.

Ryder, C. L., Marenco, F., Brooke, J. K., Estelles, V., Cotton, R., Formenti, P., McQuaid, J. B., Price, H. C., Liu, D. T., Ausset, P., Rosenberg, P. D., Taylor, J. W., Choularton, T., Bower, K., Coe, H., Gallagher, M., Crosier, J., Lloyd, G., Highwood, E. J., and Murray, B. J.: Coarse-mode mineral dust size distributions, composition and optical properties from AER-D aircraft measurements over the tropical eastern Atlantic, Atmos. Chem. Phys, 18, 17225-17257, 2018.

Seinfeld, J. H. and Pandis, S. N.: Atmospheric Chemistry and Physics: From Air Pollution to Climate Change, Wiley, 2006.

Soo, J. C., Monaghan, K., Lee, T., Kashon, M., and Harper, M.: Air sampling filtration media: Collection efficiency for respirable size-selective sampling, Aerosol Sci Technol, 50, 76-87, 2016.

Talbot, R. W., Andreae, M. O., Berresheim, H., Artaxo, P., Garstang, M., Harriss, R. C., Beecher, K. M., and Li, S. M.: Aerosol Chemistry during the Wet Season in Central Amazonia - the Influence of Long-Range Transport, J. Geophys. Res. Atmos., 95, 16955-16969, 1990.

Thomas, J. W.: Gravity Settling of Particles in a Horizontal Tube, J. Air Pollut. Control Assoc., 8, 32-34, 1958.

von der Weiden, S. L., Drewnick, F., and Borrmann, S.: Particle Loss Calculator – a new software tool for the assessment of the performance of aerosol inlet systems, Atmos. Meas. Tech., 2, 479-494, 2009.

Wendisch, M. and Brenguier, J. L.: Airborne Measurements for Environmental Research: Methods and Instruments, 2013.

Young, G., Jones, H. M., Darbyshire, E., Baustian, K. J., McQuaid, J. B., Bower, K. N., Connolly, P. J., Gallagher, M. W., and Choularton, T. W.: Size-segregated compositional analysis of aerosol particles collected in the European Arctic during the ACCACIA campaign, Atmos. Chem. Phys, 16, 4063-4079, 2016.

Zender, C. S., Bian, H. S., and Newman, D.: Mineral Dust Entrainment and Deposition (DEAD) model: Description and 1990s dust climatology, Journal of Geophysical Research-Atmospheres, 108, 2003.

1012 **Figures**
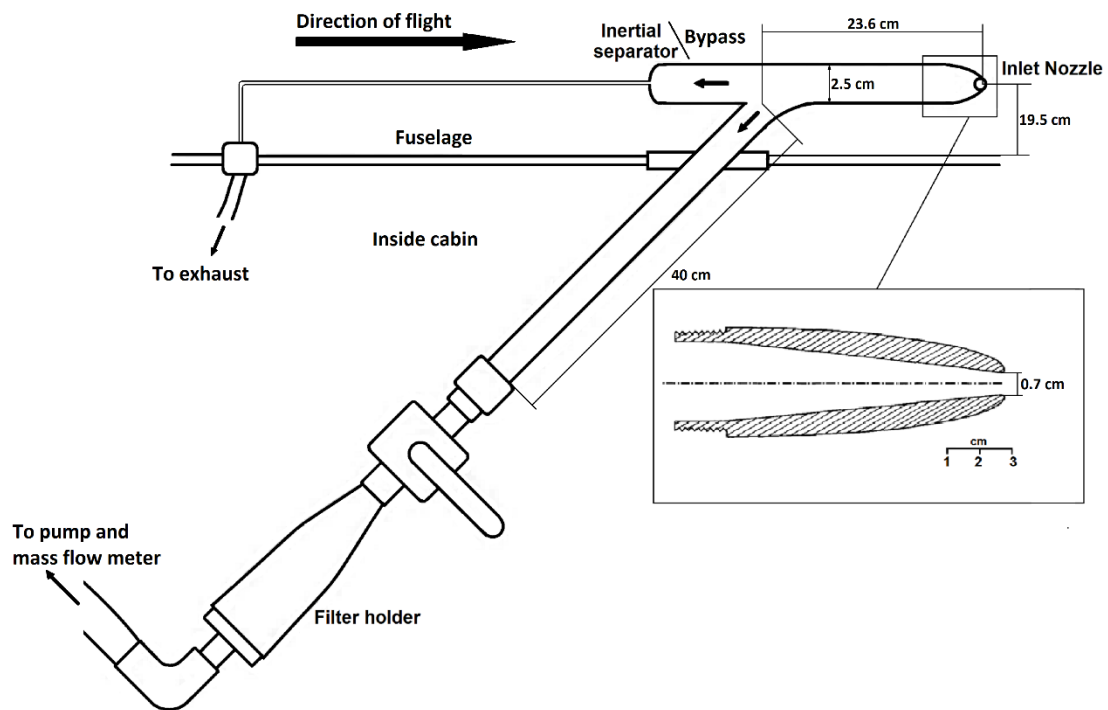
1013

1014   Fig. 1. Schematic diagram of one of the two parallel lines of the Filters inlet system.
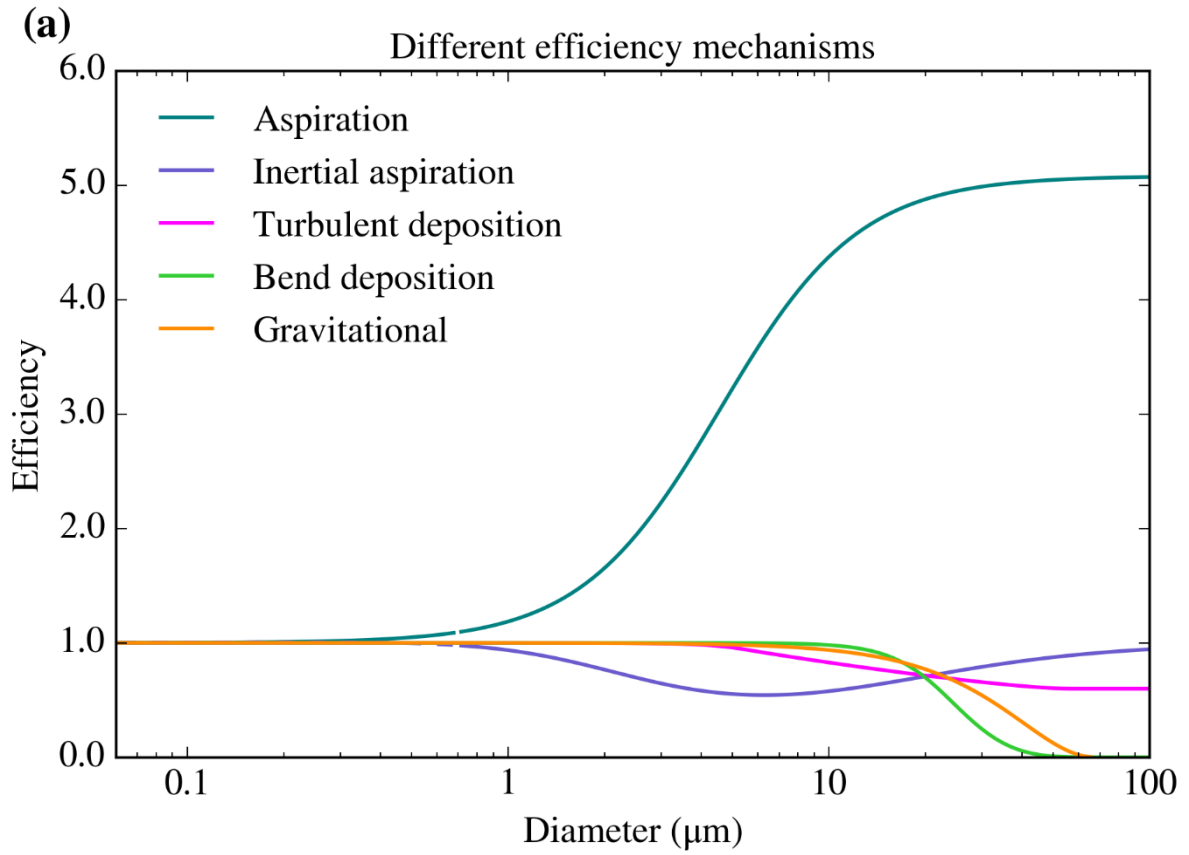
1015
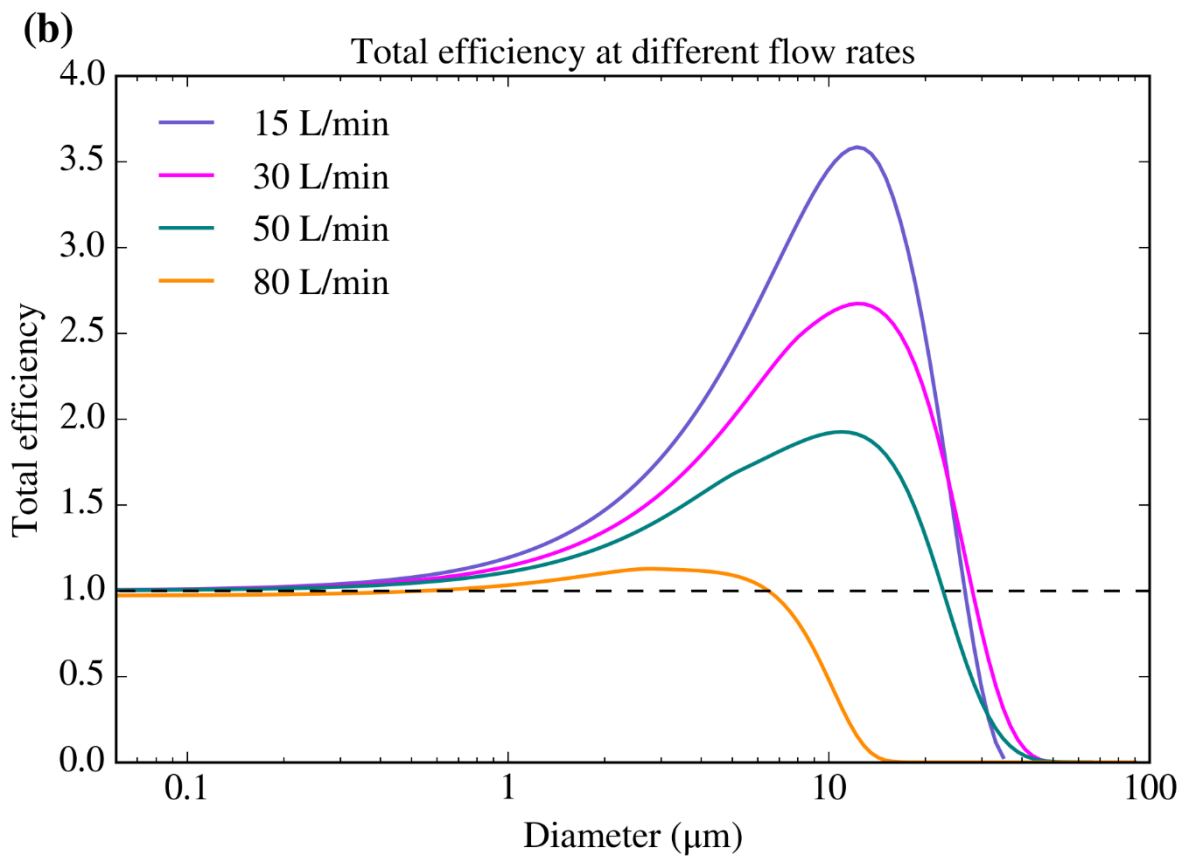
1016
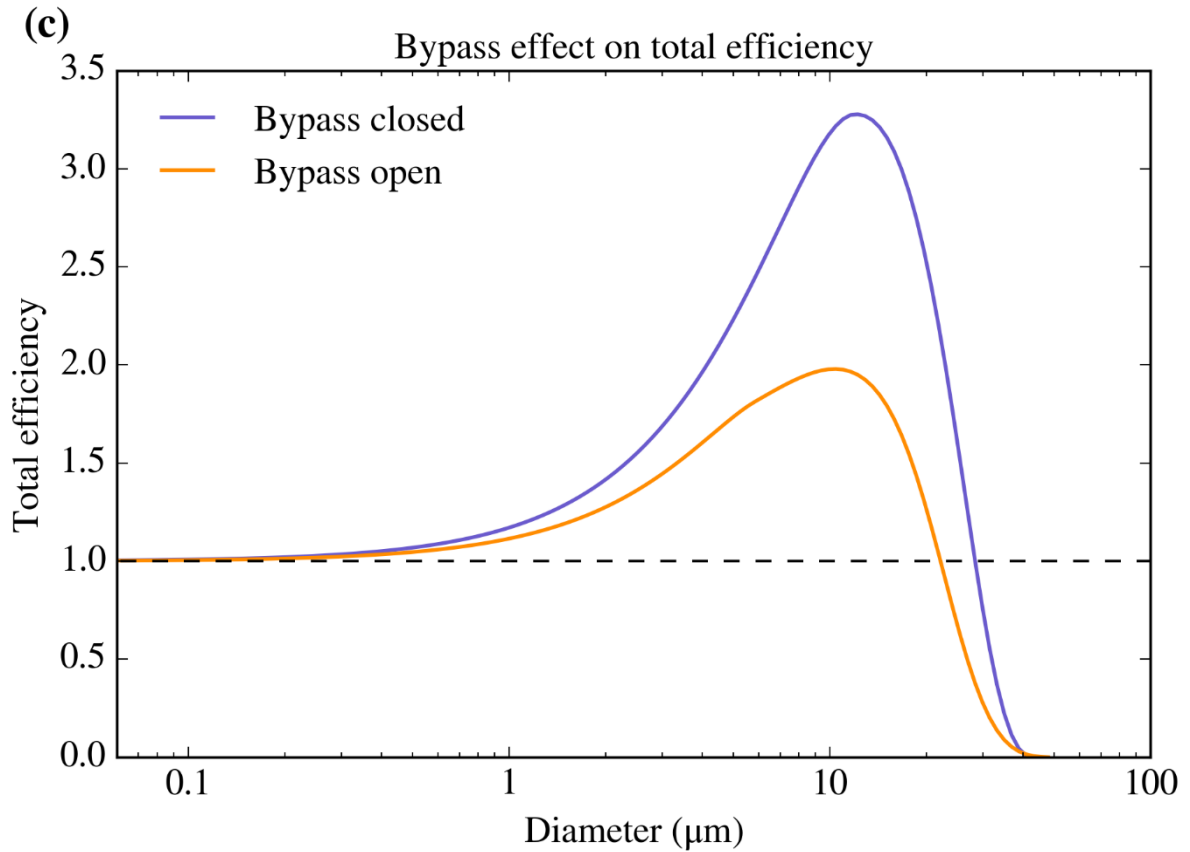
Fig. 2. *Theoretical efficiencies of the Filter inlet system.* (a) Efficiencies of the four mechanisms considered in this work for a total flow rate of 50 L min^{-1}. We have assumed a dynamic viscosity of 1.82x10^{-5} kg m^{-1} s^{-1} (value for 0 °C) and a particle density of 1000 kg m^{-3}. The speed of the air mass (U$_0$) was 110 m s^{-1}, a typical FAAM flying speed at low altitudes. (b) Total efficiency for four different total flow rates. For the 80 L min^{-1} case, turbulent deposition through the whole line was considered since the flow was turbulent through the whole pipe. (c) Total efficiency considering all the described mechanisms for a 20 L min^{-1} filter flow rate with the bypass closed and a 20 L min^{-1} filter flow rate with the bypass open (considering a bypass flow of 25 L min^{-1}).
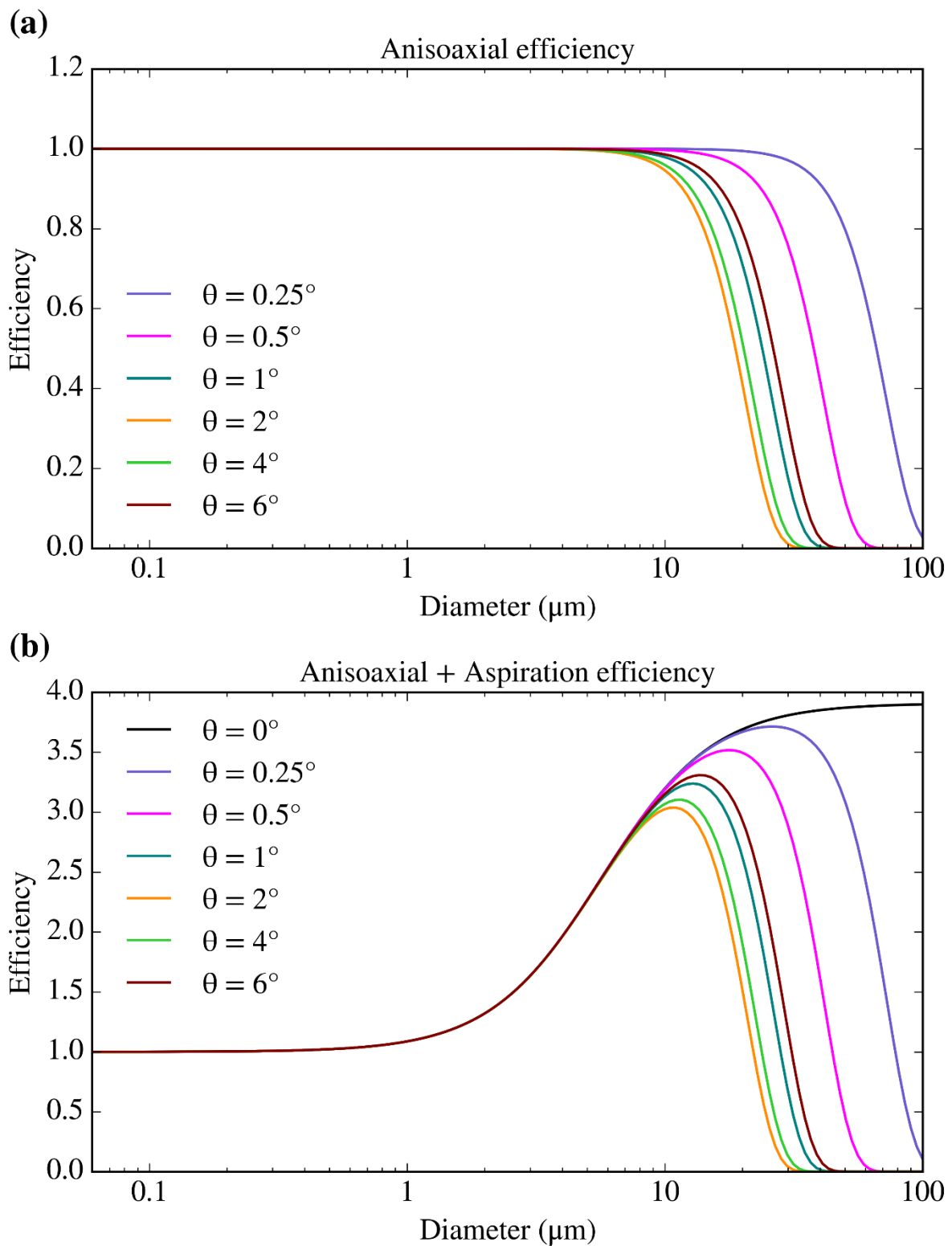
1027
1028 Fig. 3. Anisoaxial inertial losses of the sampling carried out by the Filters inlet system for different values of the angle in
1029 between the inlet and the flight direction. The calculations have been presented by themselves (a) and combined with the
1030 aspiration efficiency (b), which one can see in Fig. 2a. The anisoaxial calculations have been done using the equations given
1031 by (Hangal and Willeke, 1990b), using the same parameters and dimensions than in Fig. 2, apart from the flow rate, which
1032 was set to 65 L min^{-1} in order to be within the valid range of U/U_0 that was used to develop the equation. For smaller or
1033 larger values of the flow rate (under which most of the sampling is carried out), the differences in the efficiency from the
1034 ones show here are minimal.
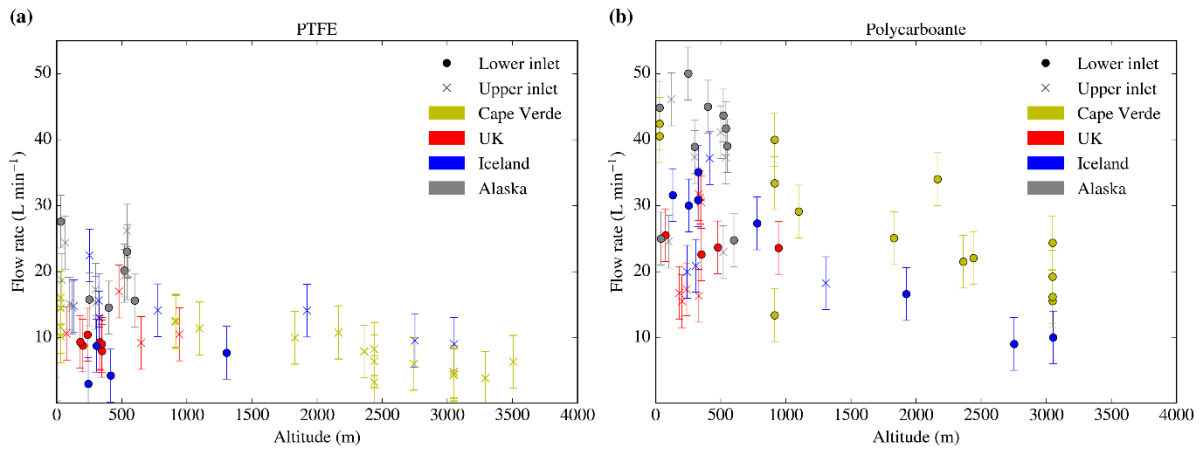
Figure 4. Filter flow rate of different samplings carried out in different campaigns at each altitude using: (a) Sartorius PTFE membrane filters (47mm diameter with a pore size of 0.45μm) and (b) Whatman nucleopore polycarbonate track etched filters (47mm diameter with a pore size of 0.4μm). The crosses represent samples taken in the upper line of the inlet system, whereas dots represent the sampling in the bottom line. Different mesh supports were used for the data collection. The data from Cape Verde was extracted from (Price et al., 2018) and the notes of the analysis carried out by the authors whereas the altitude data from the other three was obtained from the pressure altitude measurement carried out by the Reduced Vertical Separation Minimum system on board of the aircraft. The altitude data was extracted from the FAAM core datasets C019, C022, C024, C025, C058, C059, C060, C061, C062, C063, C085, C086, C087, C088, C089, C090 and C091 (via the Centre for Environmental Data Analysis). The bypass was closed for all the data in Cape Verde whereas it was open for all the data in the other campaigns. Note that the flow rate here corresponds to the filter flow rate (measured with the mass flow meter), not the total one.
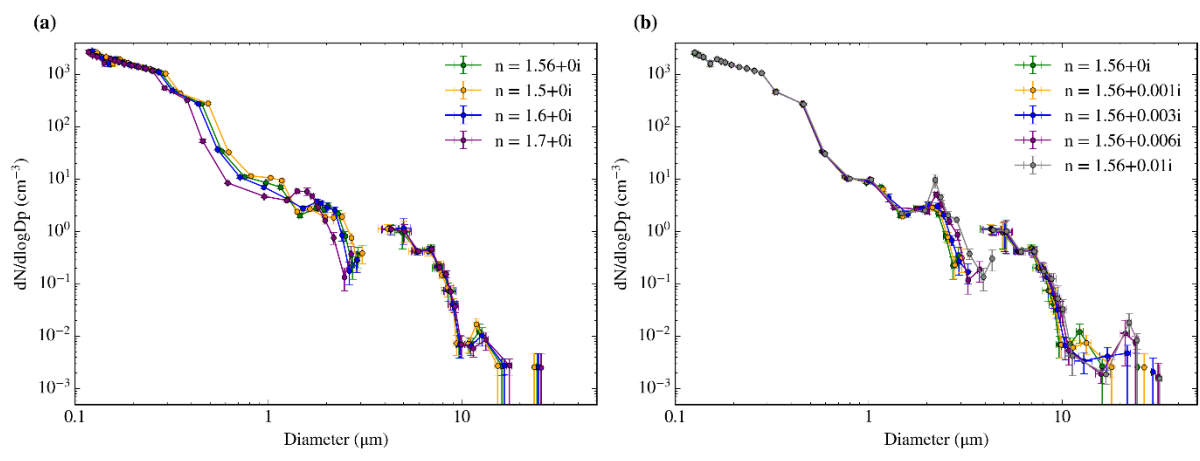
1050 Figure 5. Sensitivity of the size distributions measured by the PCASP-CDP during the C010 flight on the 2017/05/10 from
1051 11:24 to 11:38 UTC to small variations in the refractive index. We tested both the real part (a) and imaginary part (b). The
1052 errors are calculated according to the methods explained in Sect. 3.

1053
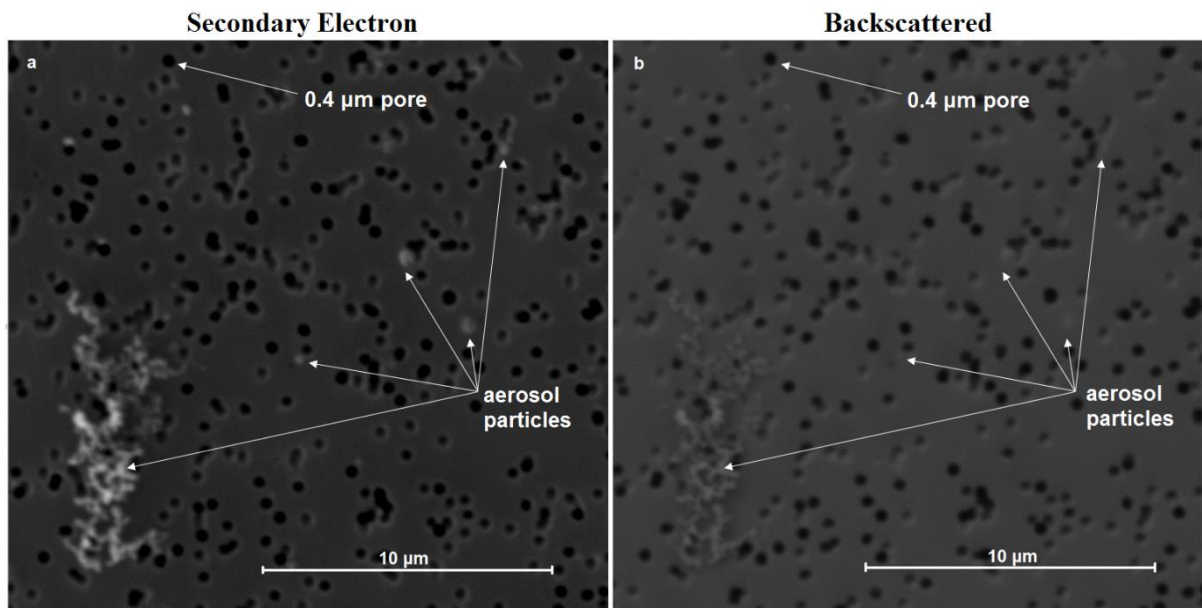
1054

Figure 6. Secondary electron image (a) and Back Scattered Electron image (b) of the same area of the same filter, collected in S.E. England on the 2018/07/05 from 13:32 to 13:47 in the upper line with the bypass open. As one can see, some of the small particles in the SE image appear almost transparent under the BSE image. Even the 10µm soot particle in the bottom left of the image shows a very low contrast in the BSE image.

1055
1056
1057
1058

1059
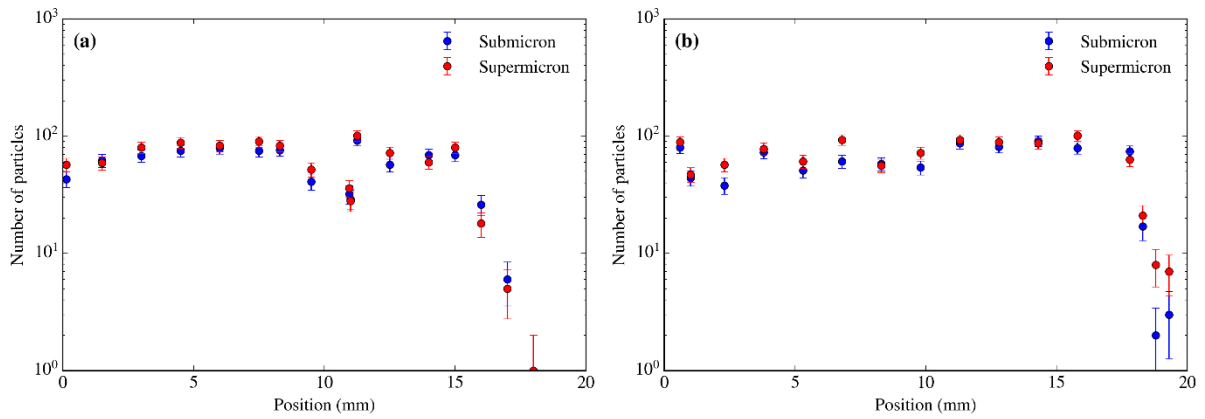
1060

1061 Figure. 7. Radial distribution of particles test on the sample collected on the 2017/10/02 (flight C059) from 16:24 to 16:40
1062 UTC about 320 m high in south Iceland, using the lower line and open bypass, sampling 432 L. Number of submicron and
1063 supermicron particles in same size areas (~160x190 μm^2) radially distributed versus the distance from the approximate
1064 centre through a radius of the filter (a) and another trajectory from the centre of the filter deviated 30° from the first radius
1065 (b). The analysis was done at 20 KeV and x5000. The number of both supermicron and submicron particles remains very
1066 constant all over the surface of the filter, until reaching the edges of it (which are cover by a rubber O-ring during the sample)
1067 and the number of particles drops to the limit of the detection within a few millimetres. The error in the number of particles
1068 comes from Poisson counting statistics.

1069

1070

1071
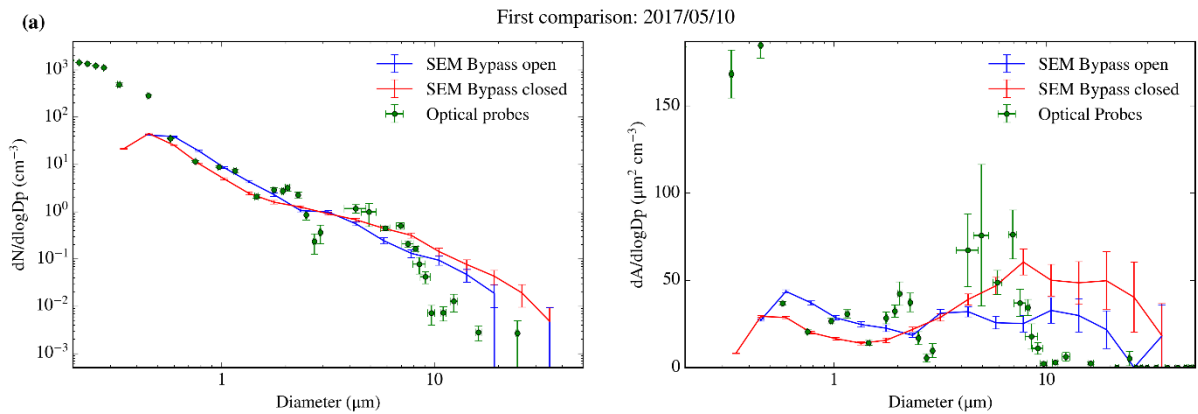
1072
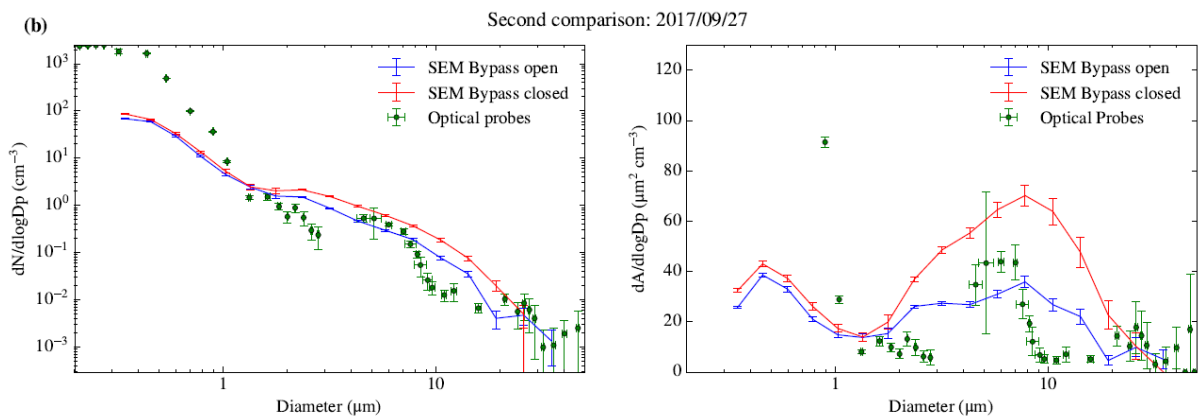
1073
1074 Figure 8. (a) First bypass test carried out during the C010 flight on the 2017/05/10 from 11:24 to 11:38 UTC. The lower line
1075 sampled 226 L with the bypass closed, whereas the upper line sampled 141 L with the bypass open at an altitude of about
1076 150 m. The flow rates were 16.1 L min^{-1} and 10.6 L min^{-1} respectively. (b) Second bypass test carried out during the C057
1077 flight on the 2017/09/27 from 13:33 to 13:50 UTC. The lower line sampled 555 L with the bypass open, whereas the upper
1078 line sampled 499 L with the bypass closed, at about 240 m. The flow rates were 34.7 L min^{-1} and 31.2 L min^{-1} respectively.
1079 The position of the closed and open line was swapped with respect to the first comparison. The sampling was interrupted
1080 for a minute to avoid a turn. Both comparisons are shown in both number size distribution and surface area size distribution.
1081 The optical probes are the PCASP-CDP, using the closest calibration to the sampling date and a refractive index of 1.56 as
1082 stated in the Sect. 2.3. The only error source considered for the SEM size distribution is the Poisson counting error.

1083

1084

1085

1086
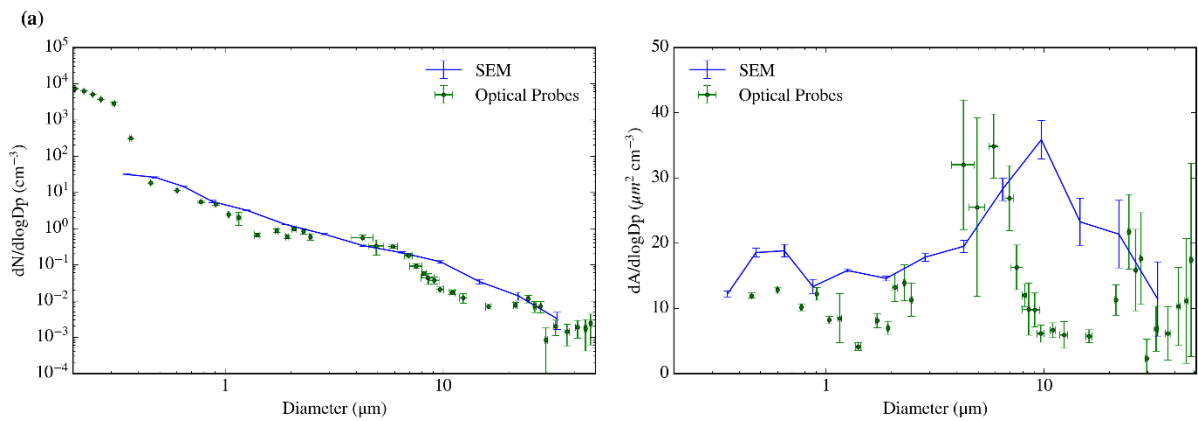
1087
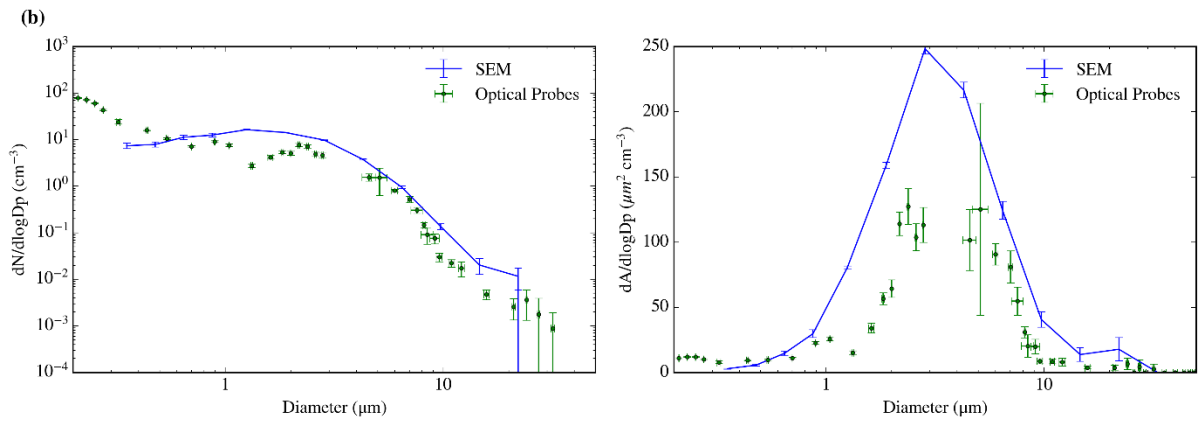
1088
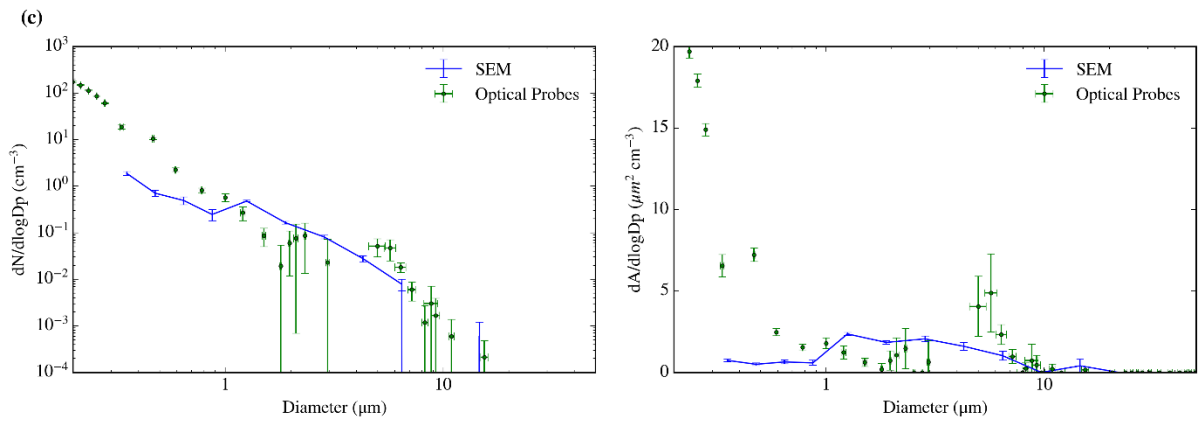
1089
1090 Figure 9. SEM obtained size distribution compared with PCASP-CDP online size distribution for three different sampling
1091 periods in three different aerosol environments. Close to London, on the 2017/07/19 (flight C024) from 15:20 to 15:51 UTC,
1092 sampling 953 L (a), south of Iceland on the 2017/10/02 (flight C059) from 16:24 to 16:40 UTC, sampling 432 L at an altitude
1093 of about 320 m, (b) and in north Alaska on the 2018/03/20 (flight C090) from 20:15 to 20:37, sampling 724 L (c). All the
1094 sampling was done in the upper line with the bypass open. The flow rates through the filter holders are 30.9, 30.5 and 42.0
1095 L min^{-1} respectively. The optical probes are the PCASP-CDP, using the closest calibration to the sampling date and a refractive
1096 index of 1.56 as stated in Sect. 2.3.

1097

(b)

1100

(c)
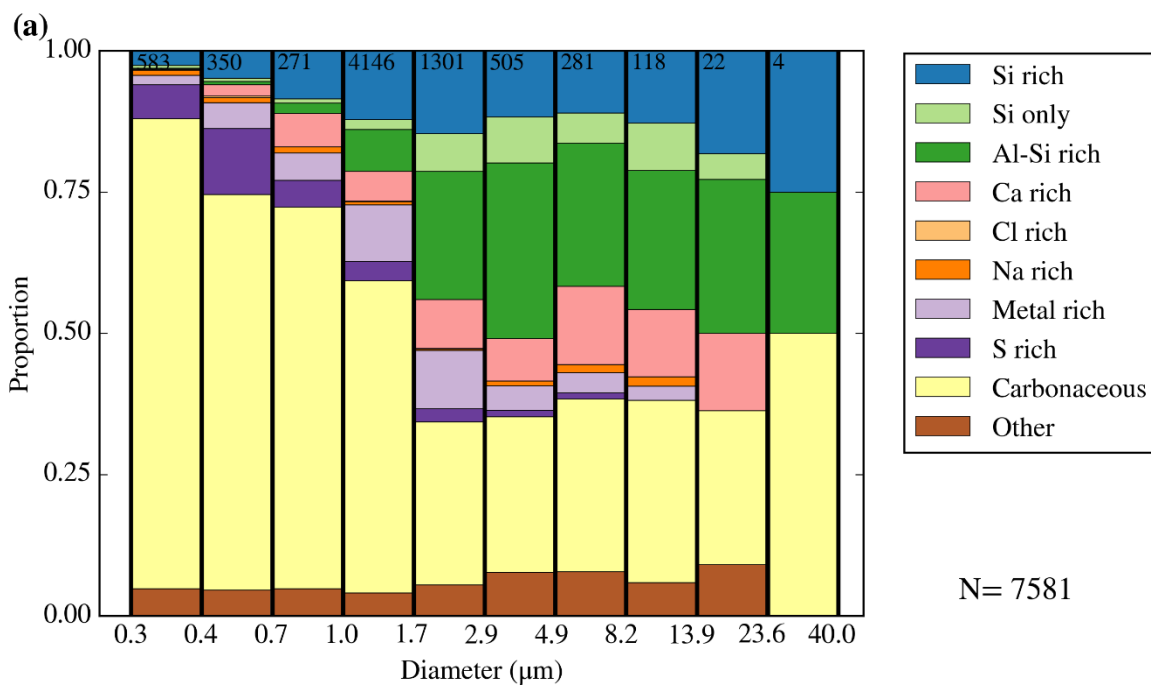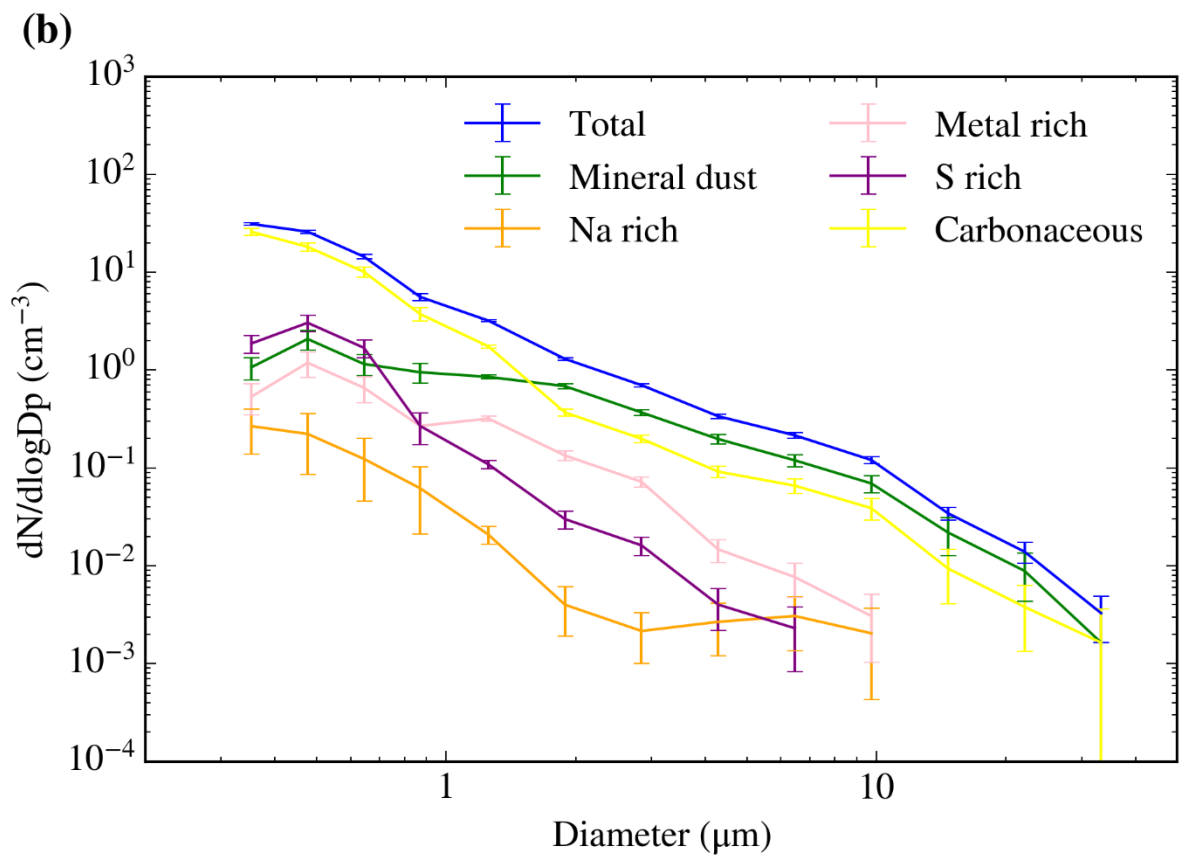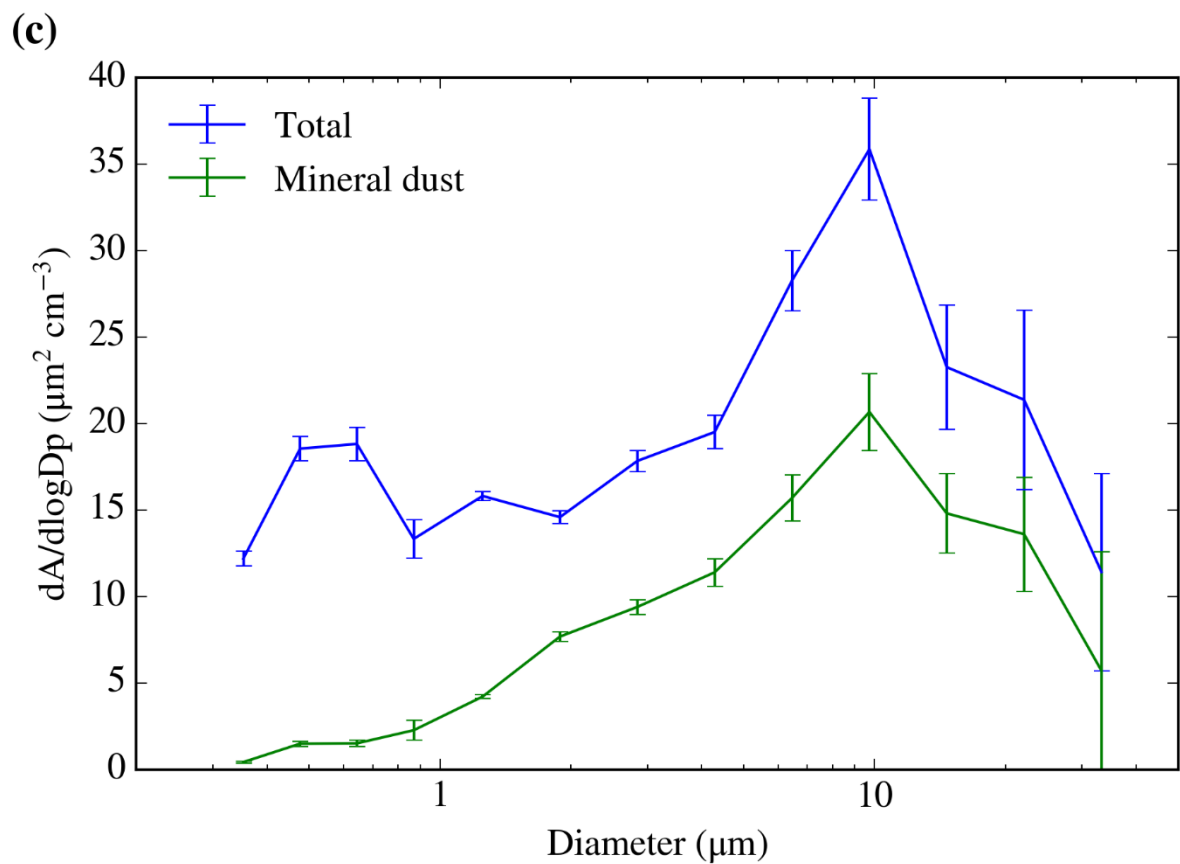
1101

1102 Figure 10. Size-segregated compositional and morphological analysis of a sample collected close to London (S.E. England) on
1103 the 2017/07/19 from 15:20 to 15:52 UTC by the lower line with the bypass open, sampling a total of 953L at 350 m altitude.

(a) Fraction of particles corresponding to each compositional category (described in the Appendix B) for each size. The number of particles per bin can be seen in the top of the figure. (b) Number size distribution for each composition. Cl rich particles were not included since only two particles in this category were found. The errors have been calculated from the Poisson counting statistics (applying it to both the size distribution and the compositional measurements). (c) Surface area of both all the detected aerosol particles and the ones whose composition was consistent with mineral dust. Errors have been calculated in the same way as before. By integrating the green curve in the figure (c) we obtained the total surface area of mineral dust in the sample (19.1 μm^2 cm^{-3}).
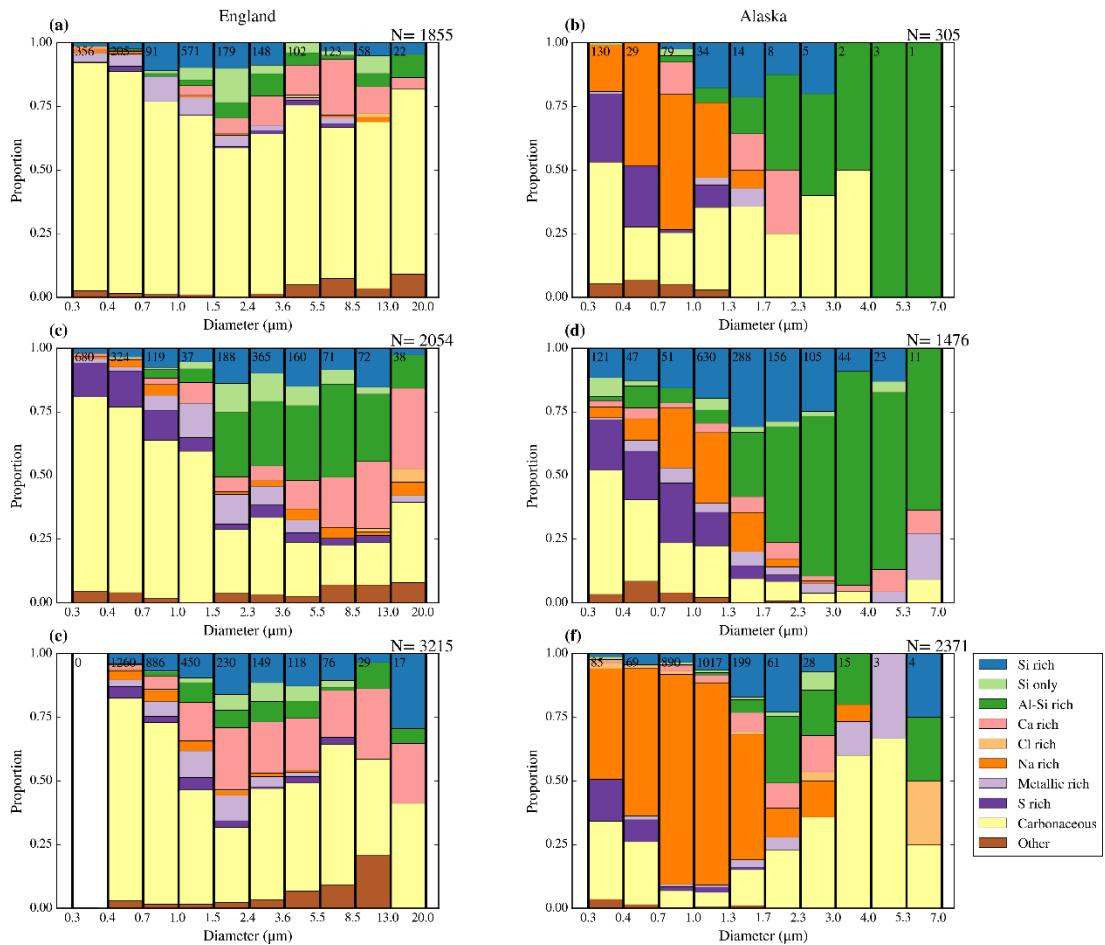
Figure 11. Six examples of the size resolved composition of aerosol sampled from the BAe-146 aircraft above South England (a, c and e) and North Alaska (b, d and f). All the samples were taken with the bypass open. The dates and sampling times (in UTC) are: (a) 2017/07/17 (flight C022) from 9:29 to 9:41, sampling a total of 182 L at an altitude of about 240 m, (b) 2018/03/18 (flight C089) from 19:28 to 19:48, sampling a total of 404 L at an altitude of about 600 m, (c) 2017/07/19 (flight C024) from 15:20 to 15:52, sampling a total of 256 L at an altitude of about 350 m (this sample was taken on the same that as the one shown in Fig. 10), (d) 2018/03/20 (flight C090) from 20:15 to 20:37, sampling a total of 724 L at an altitude of about 520 m, (e) 2017/07/20 (flight C025) from 12:51 to 13:09, sampling a total of 425 L, (f) 2018/03/21 (flight C091) from 18:27 to 18:56, sampling a total of 1187 L at an altitude of about 120 m at an altitude of about 940 m.
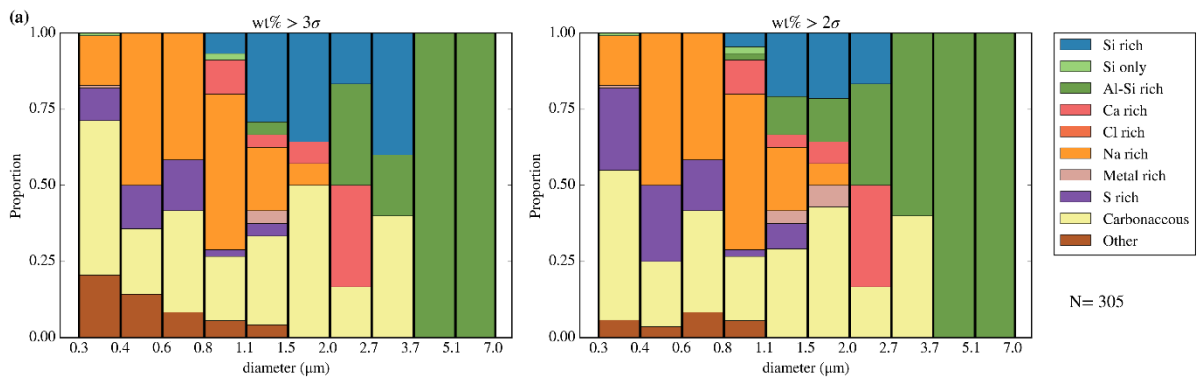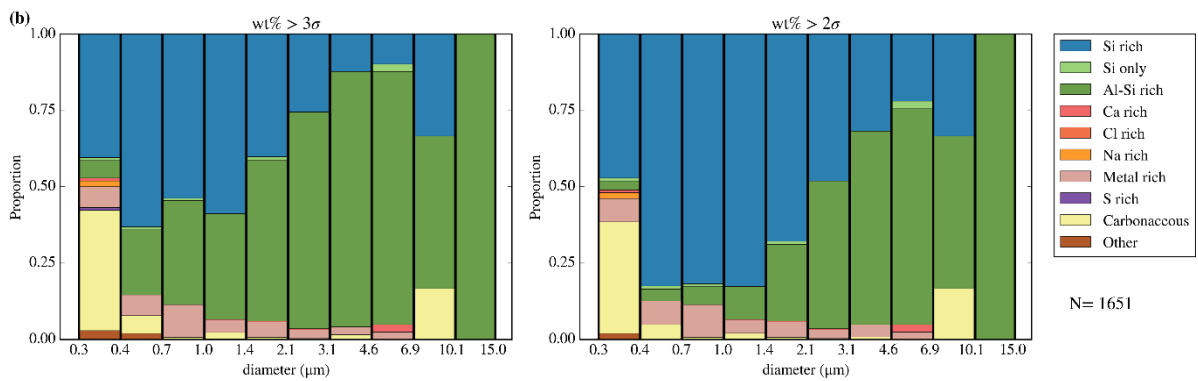
Figure C1. Size-segregated composition of two aerosol samples for different element detection confidence levels. The samples are 2018/03/18 from 19:28 to 19:48 UTC in north Alaska (a) and 2017/10/02 from 16:24 to 16:40 UTC in Iceland (b). The two samples are very different since the first sample presented a very low aerosol loading and it is dominated by Na rich particles, Carbonaceous and mineral origin aerosol (Si rich, Si only, Al-Si rich) with significant contributions of S rich particles whereas the second sample presented a high aerosol loading and it was mainly dominated by mineral origin aerosol. The different in the confidence mainly affected the Si and Al-Si rich particles as well as the S rich particles in the sample (a), whereas it only affected the Si and Al-Si rich particles in the sample (b).